Tailoring functional nanostructured lipid carriers for glioblastoma treatment with enhanced permeability through *in-vitro* 3D BBB/BBTB models

Tamara Zwain[1,2], Jane Elizabeth Alder[1.3], Bassem Sabagh[4], Andrew Shaw[1], Andrea J Burrow[1], Kamalinder K Singh[1,2,3,*]

[1]School of Pharmacy and Biomedical Sciences, Faculty of Clinical and Biomedical Sciences, University of Central Lancashire, Preston PR1 2HE, UK
[2]UCLan Research Centre for Smart Materials, University of Central Lancashire, Preston, United Kingdom PR1 2HE

[3] UCLan Research Centre for Translational Biosciences and Behaviour, University of Central Lancashire, Preston,
United Kingdom PR1 2HE

[4]Postnova Analytics UK Ltd, Unit 64, Malvern Hills Science Park, Worcestershire, WR14 3SZ, UK

*Corresponding author contact E-mail ksingh1@uclan.ac.uk

*To whom correspondence should be addressed

Professor Kamalinder K Singh
M Pharm, Ph D
School of Pharmacy and Biomedical Sciences
Faculty of Clinical and Biomedical Sciences,
University of Central Lancashire
Preston, PR1 2 HE, UK
E-mail: ksingh1@uclan.ac.uk
+44 (0) 1772 89 5843

Highlights

- Development of functional NLCs with high drug encapsulation and permeability across Blood Brain Barrier (BBB).
- Liquid lipids in the NLCs impact its permeability across the 3D *in vitro* BBB model and affects the integrity of the barrier.
- Docetaxel NLCs overcome the blood-brain tumour barrier and accumulate efficiently in the patient-derived glioblastoma cells.
- Docetaxel NLCs show G2/M phase cell arrest and enhanced efficacy in 3D tumour spheroids of U87 MG cells.

Graphical abstract

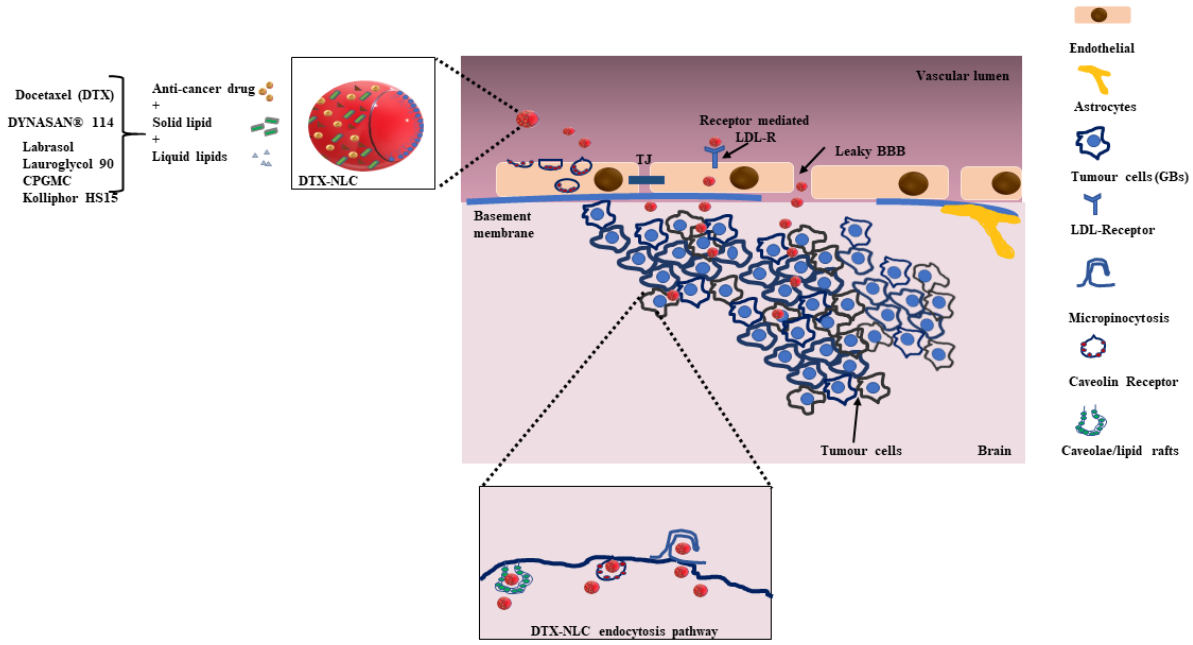

Abstract

The blood-brain barrier (BBB) and blood-brain tumour barrier (BBTB) pose a significant challenge to drug delivery to brain tumours, including aggressive glioblastoma (GB). The present study rationally designed functional nanostructured lipid carriers (NLC) to tailor their BBB penetrating properties with high encapsulation of CNS negative chemotherapeutic drug docetaxel (DTX). We investigated the effect of four liquid lipids, propylene glycol monolaurate (Lauroglycol® 90), Capryol® propylene glycol monocaprylate, caprylocaproylmacrogol-8-glycerides (Labrasol®) and polyoxyl-15-hydroxystearate (Kolliphor® HS15) individually and in combination to develop NLCs with effective permeation across *in-vitro* 3D BBB model without alteration in the integrity of the barrier. With desirable spherical shape as revealed by TEM and an average particle size of 123.3 ±0.642 nm and zeta potential of -32 mV, DTX-NLCs demonstrated excellent stability for six months in its freeze-dried form. The confocal microscopy along with flow cytometry data revealed high internalisation of DTX-NLCs in U87MG over SVG P12 cells. Micropinocytosis was observed to be the one of the dominant pathways for internalisation in U87MG cells while clathrin-mediated pathway was more predominant in patient-derived glioblastoma cells. The NLCs readily penetrated the actively proliferating peripheral cells on the surface of the 3D tumour spheroids as compared to the necrotic core. The DTX-NLCs induced cell arrest through G2/M phase with a significant decrease in the mitochondrial reserve capacity of cells. The NLCs circumvented BBTB with high permeability followed by accumulation in glioblastoma cells with patient-derived cells displaying ~2.4-fold higher uptake in comparison to U87MG when studied in a 3D *in-vitro* model of BBTB/GB. We envisage this simple and industrially feasible technology as a potential candidate to be developed as GB nanomedicine.

Keywords: Glioblastoma, blood-brain barrier, blood-brain tumour barrier, docetaxel, nanostructured lipid carrier, liquid lipids

1. Introduction

Glioblastoma (GB) is a general term used to characterise a tumour that originates from glial brain cells that represent a heterogeneous group of malignancies of the central nervous system (CNS) [1]. GB is the most common primary malignant brain tumour among the adult population, making up 46% of all the malignant brain and central nervous system tumours and 15% of all primary brain tumours [2]. Docetaxel (DTX) has shown profound benefits in the treatment of various types of cancers (breast, head and neck, prostate, and gastric carcinoma) [3,4], with the commercial dosage form Taxotere® licensed by Sanofi-Aventis and approved by the FDA [5]. Though DTX has shown to successfully inhibit brain tumour growth following local injection in a mouse brain tumour model [6], it has not been applied to treat brain metastases or primary tumours as it is subject to P-glycoprotein (P-gp) efflux at the blood-brain barrier (BBB) and consequently is unable to accumulate in the brain at adequate concentrations required for tumour regression [7]. Though blood brain-tumour barrier (BBTB) is considered more permeable than the blood-brain barrier (BBB), the former has shown to have highly functional efflux transporters and barrier properties [8]. GBs have reported displaying clinically significant regions of the tumour with an intact BBB resulting in disparate and restricted delivery of cancer therapeutics and treatment failure [9]. Thus, new drug delivery modalities are needed for circumvention of BBTB and effective treatment of GB [10].

Nanoparticulate carriers, with their nanoscale dimensions and unique properties, are being investigated as delivery systems for CNS therapeutics. Nanostructured lipid carriers (NLC), a second-generation lipid nanocarrier has received a lot of attention in recent years because of its biocompatibility, good tolerability and safe application for human use. NLCs represent promising carrier to deliver drugs to the brain due to their small size and lipidic nature [11]. Comprising of solid and liquid lipids as core matrix, they were proposed to overcome the limitations of solid lipid nanoparticles (SLN) [12] by making the structure of solid lipid less organised by addition of liquid lipid and thus to enable incorporation of higher drug payloads [13]. NLCs are amenable to large scale production without the use of organic solvents, thus making them attractive to industry. Excellent long-term stability, ease of lyophilisation and sterilisation are other value-added features of NLCs [14].

It is well known that liquid lipids present in the NLCs as oil nano-compartments enhance the solubility of the drug and prevent drug leakage on storage [15]. The nature and type of liquid lipid incorporated also

influence the size, surface morphology and stability of the particles [15, 16]. However, less attention has been paid to the role of these liquid lipids on the permeation of NLCs across the BBB. In the present research, we rationally designed functional NLCs to tailor their BBB penetrating properties coupled with high drug encapsulation in their core matrix. We investigated the effect of four liquid lipids polyoxyl-15-hydroxystearate Kolliphor® HS15 (KHS15), caprylocaproylmacrogol-8-glycerides Labrasol® (LB), Capryol® propylene glycol monocaprylate (CPGMC) and propylene glycol monolaurate Lauroglycol® 90 (LG90) individually and in combination to develop NLCs with effective permeation across BBB which would circumvent BBTB and effectively accumulate in GB cells. Kolliphor® HS15, a mixture of PEG 660 hydroxy stearate and free PEG 660 is a potent non-ionic solubiliser for poorly soluble drugs [17]. NLCs constituting of KHS15 have shown enhanced drug accumulation in the brain [18,19]. KHS15 has also been reported to prolong the circulation time of nanoparticles, which can lead to higher drug levels in the brain due to protection from biological degradation [20]. It is also known to inhibit P-gp drug efflux, which is one of the major limiting factor of poor drug transport across BBB [21]. Along with KHS15, Labrasol, a PEGylated alkyl glyceride also has the ability to inhibit the P-glycoprotein function and increase membrane permeability and opening of tight junctions [22,23]. This has been attributed to their ability to insert themselves between the plasma membrane lipid tails of the lipid bilayer and fluidise the membrane [24]. NLCs containing CPGMC as liquid lipid has shown improved brain delivery via nasal route [25]. Additionally, CPGMC has exhibited high solubility for the practically insoluble drug DTX making it an attractive liquid lipid for further investigation [26]. LG90, well known as permeation enhancer and for its drug solubilisation properties was also one of the excipients in the NLC formulation employed for nose to brain drug delivery [27]. Therefore, the present study investigated these four liquid lipids known for their permeation enhancement [22,28] for the formulation of DTX-NLCs and screened them using all human 3D *in vitro* BBB model [29,30], to demonstrate the impact of liquid lipid in the NLCs on its BBB permeation.

The optimised NLCs with a combination of liquid lipids which showed desirable BBB permeability and efficient DTX loading were fully characterised for particle size, asymmetric field-flow fractionation, transmission electron microscopy, x-ray diffractometry, thermogravimetric analysis, differential scanning

calorimetry, Raman spectroscopy and Fourier-Transform Infrared Spectroscopy. The DTX-NLCs were appraised for their suitability to be developed as a future therapeutic intervention for GB by evaluating their effect on immortalised GB cell lines and short-term GB patient-derived culture and assessed for cell uptake, mechanism of cellular internalisation, cell proliferation, cell cycle arrest and cell respiration for their mitochondrial effect. In addition, the developed NLCs were evaluated through 3D tumour spheroids and the *in vitro* disease model of BBTB/GB. We envision this simple and industrially feasible technology as a potential candidate to be developed as GB nanomedicine. In the present study, we have demonstrated that novel functional NLCs with an optimised mixture of liquid lipids demonstrate increased BBB permeability *in vitro* and improved efficacy in 3D tumour spheroids and BBB/BBTB *in vitro* models.

2. Materials and methods

2.1. Materials

2.1.1 Chemicals and reagents

Dynasan®114 gift sample from CREMER OLEO, UK, Phospholipon 90H, and Lipoid S75 free samples from Lipoid, Germany. Labrasol®, Lauroglycol 90 and Capryol propylene glycol monocaprylate were a kind gift from Gattefossé, France. Docetaxel was purchased from Kemprotec, UK. Sodium cholate, Kolliphor®HS15, Propidium iodide and Evans blue dye (EBD) and agarose were purchased from Sigma Aldrich, UK. Eagle's minimum essential medium (EMEM) Human serum (HS), Endothelial basal media (EBM-2)/(EGM-2), Astrocyte basal media (ABM-2)/(AGM-2) kits were purchased from Lonza, Belgium and pericyte medium (PM), was purchased from Caltag Medsystems.

2.1.2. Cell lines

SVG P12 (human, non-cancerous foetal glial cell line), U87MG (human glioblastomas, grade IV cell line) and RAW 264.7 (macrophages) from the European Collection of Cell Cultures (ECACC, UK). BTNW911, a short-term culture derived from primary cells obtained from a 60-year-old male grade IV glioblastoma, with written ethical consent from the Brain Tumour North West (BTNW) tissue bank (Supplementary data). Human microvascular endothelial cells (HMBEC), human brain vascular pericytes (HBVP), and human astrocytes (HA) were purchased from (Sciencell, Buckingham, UK). Cells were incubated in a humidified incubator under 5% CO_2 at 37°C for culturing.

2.2. NLC Optimisation and *in vitro* BBB permeability

2.2.1. Docetaxel nanostructured lipid carrier (DTX-NLCs) preparation and optimisation

Four NLC dispersions with each of the four liquid lipids, Labrasol® (B1), Lauroglycol 90 (B2), CPGMC (B3) and Kolliphor® HS15 (B4) and one containing a blend of four liquid lipids (B5) as per the compositions given in Table 1 were prepared using hot homogenisation technique [31].

Briefly, DTX (100 mg), solid lipid Dynasan®114 (4 g), Phospholipon 90 H (300 mg), and the liquid lipids were melted under a controlled temperature (80°C) followed by addition of Lipoid S75 (2.4 g) to the lipid phase. The aqueous phase composed of sodium cholate (374 mg) and 100 ml water maintained at 80°C, was added to the lipid phase under continuous stirring and mixed for 20 minutes to form a pre-emulsion. The pre-emulsion was placed in ice-bath, and the mixture was sonicated using a Probe sonicator (Vibra Cell Sonics, USA) [32,33] and left to cool down to obtain the NLCs. The same method was used to prepare the Blank-NLC (B-NLC), where DTX was not added, while for rhodamine 123 (R123) labelled NLCs (R-DTX-NLCs) the fluorescent dye was added to the melting lipid phase, and the same process was followed. Dynamic light scattering (DLS) technique was used to obtain the particle size, polydispersity index (PDI), and zeta potential (ZP) for all the developed NLCs using Zeta Sizer (Malvern Zetasizer Nano, Panalytical Instalment Ltd, UK) at 25°C. High-pressure liquid chromatography (HPLC) (Agilent HPLC 1260 Infinity, Agilent Technologies, USA), was used to quantify DTX concentration in the NLCs using a C18 column (Luna 5µm, PFP (2), 100Å, 250 x 4.6 mm, Phenomenex, UK) set at 40°C with a mobile phase consisting of acetonitrile and water (50:50, v/v) at a flow rate of 1.0 ml/min and detected at 230 nm. The entrapment efficiency (EE) was determined by quantifying un-entrapped DTX in the supernatant separated by filtering NLCs (0.5ml) using Amicon 3 kDa molecular cut-off centrifuge filters centrifuged at 15600 x g for 60 min. EE was computed by equation 1 [34]. Total drug (TD) and drug loading (DL) was determined by dissolving the NLCs in tetrahydrofuran (THF), and suitability diluted with acetonitrile and water (50:50, v/v) and analysed for DTX content and calculated using equations 2 [34] and 3 [35] respectively.

$$\% \, \boldsymbol{EE} = \left\{\frac{\boldsymbol{TD-FD}}{\boldsymbol{TD}}\right\} \times \mathbf{100} \text{ (Equation 1)}$$

$$\% \, \boldsymbol{DL} = \left\{\frac{\boldsymbol{mass\ of\ DTX}}{\boldsymbol{mass\ of\ Lipids\ in\ the\ NLCs + mass\ of\ DTX}}\right\} \times \mathbf{100} \text{ (Equation 2)}$$

$$\% \, \boldsymbol{TD} = \left\{\frac{\boldsymbol{DTX\ concentration\ after\ processing}}{\boldsymbol{DTX\ added\ concentration\ before\ processing}}\right\} \times \mathbf{100} \text{ (Equation 3)}$$

2.2.2. Permeability across 3D *in vitro* BBB model

Three primary derived cell lines were grown and seeded as per the published protocol [30], to set up an all human tri-culture 3D *in vitro* BBB model. Briefly, the cells were seeded on the apical outer and inner part of the insert and incubated for 48 h at 37°C in a humidified incubator under 5% CO_2. The transendothelial electrical resistance (TEER) on the insert was measured using the EVOM-2 meter (Merck Millipore, UK) every day, for 7 days to ensure the formation of BBB. On day 8, the model was used to determine the permeability of the five NLC formulations (B1, B2, B3, B4, and B5) labelled with R123. The TEER value was measured to evaluate tight junction (TJ) opening [30,36], and fluorescence was measured at λ_{Ex} 485 nm, and λ_{Em} 535 nm using a plate reader (Genios Pro microtiter plate reader, Tecan, Austria) to monitor the concentration of the NLCs permeated to the basal side. Apparent permeability (Papp) was determined using equation 4.

$$\boldsymbol{P_{app}} = \left(\frac{\boldsymbol{V}}{\boldsymbol{A \times C_0}}\right) \times \left(\frac{\boldsymbol{dQ}}{\boldsymbol{dt}}\right) \text{ (Equation 4)}$$

where: V = Volume of basolateral compartment (0.5 cm^3), A = surface area of the polycarbonate membrane (0.3 cm^2), C_0 = Concentration of formulation in the apical side (1µg/ml), dQ Change in the concentration of formulation passing across the cell layer to basolateral side (µg/ml), dt = Change in time (Sec).

The integrity of the barrier was tested using Evans-blue dye (EBD) prior and at the end of each experiment to ensure that the model was intact during the entire experiment.

2.3. DTX-NLCs physicochemical characterisation

2.3.1. Transmission electron microscopy (TEM), asymmetric Flow Field-Flow Fractionation (AF4) and Nanoparticle Tracking Analysis (NTA)

TEM was carried out to study the morphology of DTX-NLC and B-NLC. The samples were put on the glow discharged carbon-coated copper grid (300 mesh). The grids were briefly washed with distilled water and stained with 1% of uranyl acetate in water before blotting. Images were taken at FEI Tecnai 12 Biotwin

microscope at 80kV accelerating voltage using Gatan Orius SC1000 CCD camera. To obtain accurate particle size and particle size distribution, AF4 was performed using an AF2000 Multiflow system (Postnova Analytics) equipped with three online detectors: A 21 angle, multi-angle light scattering detector (MALS, Postnova Analytics), a Zetasizer Nano ZSP dynamic light scattering detector (DLS, MalvernPanalytical) and a dual-wavelength UV detector (UV, Postnova Analytics) set for these experiments at 280 nm and 230nm. For the separation, an analytical AF4 channel (Postnova Z-AF4-CHA-611) with a 350 μm spacer defining the channel height was used with a regenerated cellulose membrane with nominal 10 kDa cut-off (Postnova Z-AF4-MEM-612-10KD). The temperature was set at 30°C and samples were eluted with HPLC grade water with 0.02% NaN_3 filtered at 0.1 μm using a time delay exponential decay for the cross-flow and a constant detector flow of 0.5 mL min^{-1}. Data were analysed by NovaFFF software version 2.1.0.5 (Postnova Analytics).

Further to verify the results of DLS, mean particle size and particle distribution was also determined by Nanoparticle tracking analysis NTA (Nano Sight NS300 Malvern Panalytical, UK) equipped with a scientific CMOS camera, a blue laser module 488 and NTA software 3.3. A 1-ml disposable syringe was used to inject the samples into the instrument chamber at syringe pump speed set at 70. The detection threshold of the NTA software was set to 4, and the maximum jump distance and the minimum track segment length were both set to auto.

2.3.2. *In vitro* DTX-NLCs release

The release of DTX from DTX-NLC was evaluated in phosphate buffer saline (PBS) pH 7.4 containing 30 % (v/v) ethanol as release media [37]. 2 ml of the DTX-NLCs or DTX dispersed in 1% Tween 80 was placed in the dialysis membrane tubing (molecular weight cut-off 3.5 kDa) with both ends of the tubing secured and immersed in 400 ml of release media at 37°C under horizontal shaking (100 rpm/min). Samples (1 ml) were withdrawn at the predetermined time points (0.5, 1, 2, 4, 6, 8 and 24 h) and analysed by an HPLC method developed and validated for this purpose.

2.3.3. X-ray diffractometer (XRD)

Crystalline structures were tested by Bruker powder XRD for surfactants sodium cholate, Phospholipon 90, solid lipid Dynasan 114, DTX, physical mixture (DTX+ D114), and DTX-NLC (freeze-dried). Samples

were scanned through (5-50)° with a scanning rate of 5°/minute, with a scan type coupled two theta/theta using Scintillation counter and 1-dimensional LYNXEYE detector, A Cu-Kα radiation source-detector was used exposing samples to Cu Kα radiation (30 kV, 10 mA) [35].

2.3.4. Thermogravimetric analysis (TGA)

Thermal behaviour of DTX, Dynasan 114, B-NLC and freeze-dried DTX-NLC was determined to assess the samples stability, where each sample was heated from 25-500°C using TGA Q500. Approximately 10 mg of each sample was placed in a platinum pan and analysed for percent weight loss as a function of temperature. The collected data were analysed using TA Universal Analysis software (TA Instruments, Elstree, UK).

2.3.5. Differential scanning calorimetry (DSC)

Thermal behaviour of DTX-NLC and B-NLC was determined on DSC Q2000 TA (Thermal Analysis Instruments, UK) and compared with Dynasan 114 and native DTX. A sample of approximately 5mg was placed in a hermetically sealed Tzero pan, and an empty pan was used as a reference. Samples were analysed using heat/cool/heat run cycled between 0-240°C under a nitrogen purge of 50 ml/minute at a heating rate of 10°C /minute. The collected data were analysed using TA Universal Analysis software.

2.3.6. Fourier-Transform Infrared Spectroscopy (FTIR)

The interaction between the materials and the polymorphic state was measured using FTIR (Nicolet iS 10 FTIR, Thermo Scientific, UK). Powdered DTX was investigated against DTX-NLC and B-NLC. Samples were measured for percent transmittance in the range of 400-4000 cm^{-1} using diamond crystal and a resolution of 0.5 cm^{-1} and accumulation of 150 scan. The data were analysed using the OMNIC software (Thermo Scientific, UK).

2.3.7. Raman spectroscopy (RS)

DTX-NLC were characterised by RS (Horiba HR800 Raman), adjusted on the green laser at (532 nm) with a grating of 600; 50X magnification for the objective lens and laser intensity of 0.01%. The samples were placed on a slide wrapped with aluminium tin in a range of 400- 2000 cm^{-1}. The machine was calibrated using high purity silica wafer with a distinguishable scattering at 520 cm^{-1} prior to analysis. LabSpec 6 software was used to analyse the data.

2.3.8. Colloidal stability

Colloidal stability of DTX-NLC was assessed in different physiological media (PBS, EMEM, 5%, dextrose normal saline and distilled water). 1 ml of DTX-NLC was placed in individual glass containers and diluted with 30 ml of the test media. Samples were stored at 37°C, and aliquots were withdrawn at 0.5, 1, 2, 4, 6, 8 and 24 hours and evaluated for the changes in the particle size and PDI [38].

2.3.9. Short and long-term stability

The short-term stability of the DTX-NLC and B-NLCs were evaluated by storing the NLCs as aqueous dispersion at room temperature for three months. Samples were withdrawn periodically after 1, 2 and 3 months. While for long-term stability a freeze-dried form of DTX-NLCs were stored at -20°, 4°, 25°, and 40°C up to six months in sealed glass containers and assessed periodically after 0, 1, 3- and 6-months following reconstituting with purified water.

2.4. *In vitro* cell lines studies

2.4.1. Qualitative and quantitative cellular internalisation study

For qualitative cell internalisation, images were captured and analysed on a Zeiss confocal microscope and Zen blue software (GmbH, Germany) was used for the analysis. Briefly, the U87MG and SVG P12 cells were seeded on a sterile coverslip, placed in a 12-well plate and incubated at 37°C and 5% CO_2 to allow cells attachment. Following 24 h of incubation, the cells were removed from the incubator and washed twice with PBS (0.1 M, pH7.4). The culture media was replaced with a fresh media containing (R-DTX-NLC) prior to 4 h incubation. The cells were then washed three times with PBS, and the fluorescent images were captured after fixation in 4% of paraformaldehyde and staining with DAPI.

For quantitative time-dependent uptake, following seeding the cells, a fresh media containing R-DTX-NLC was replaced at 0.5, 1, 2, 4, 6 and 24 h for BTNW911, U87MG and SVG P12 cells, and at 4 and 6 h for the RAW 264.7 cells and 3D U87MG spheroids respectively. While for concentration-dependent studies, four-level concentrations 1, 2, 3, and 5 µg/ml were tested for U87MG and SVG P12 at 6 h. At each designated time point, the plates were washed three times with PBS (0.1M, pH 7.4), followed by trypsinisation and centrifugation at 179 x g for 5 min, then the cell pellets were resuspended with ice-cold PBS. Each sample was placed in a V-shaped, non-tissue culture 96 well plates and propidium iodide (50

µg/ml stock) was added to each well, and the fluorescence intensity was detected by flow cytometry (Guava, Merck, Germany). Non-treated cells were used as control.

2.4.2. Quantitative and qualitative endocytosis pathways analysis

The U87MG, SVG P12, and BTNW911 cell lines were exposed to different endocytosis inhibitors diluted with media, 0.45 M sucrose (clathrin pathway), 5 µg/ml cytochalasin B (micropinocytosis/phagocytosis), 5 µg/ml nystatin (caveolae/ lipid rafts pathway) and 4°C used for energy-dependent endocytosis, then 90 min later a fresh media containing endocytic inhibitors and (R-DTX-NLC) were added to the cells and incubated for further 4 h. Samples were analysed for qualitative uptake using fluorescence microscope and quantitative uptake using flow cytometer following protocol detailed in sections 2.4.1.

2.4.3. Evaluation of DTX-NLCs uptake *in vitro* BBTB model with U87MG and BTNW911

BBB is known to alter in the presence of brain tumours but still represents a significant impediment and restricts delivery of chemotherapeutic drugs to the brain and malignant tumours. To simulate the *in vivo* conditions glioma cells were placed in the basolateral side of the *in vitro* BBB model as illustrated in Fig 6a. The permeability of NLCs across the BBTB and uptake by the glioma cells was determined. Briefly, the U87MG or BTNW911 cells were seeded on the basolateral side in the wells a day before the BBB triculture reached TEER of 260 Ω/ cm^2. The inserts with triculture BBB layers were transferred to each well containing either U87MG or BTNW911 monolayer and incubated for 2 h at 37°C in a humidified incubator under 5% CO_2. The TEER was monitored, and 200 µl of R-DTX-NLC was added on the apical side when the TEER increased to ~ 300 Ω/ cm^2. Samples were withdrawn at 1, 2, 4 and 6 h from the basolateral side of the insert and the fluorescence was measured using the plate reader Tecan GENios Pro® plate reader. At 6 h U87MG/ BTNW911 cells were collected and analysed for uptake using the flow cytometer following the protocol detailed in section 2.4.1. The Papp was determined using equation 4.

2.4.4. Cell proliferation evaluation of DTX-NLCs in 2D cell lines and 3D spheroids

The U87MG, SVG P12, and BTNW911 cells were seeded and cultured for 24 h prior to treatment with B-NLC, DTX-NLC and DTX at concentrations ranging from 2.5 to 1000ng/ml. Media without any cells was used as a blank, and cells and media without a drug were used as a control. Presto Blue® was used to perform the proliferation assay following 72 h incubation with treatment. Fluorescence response for Presto

Blue was quantified at an λ_{Ex} of 535 nm and λ_{Em} of 612 nm following incubation for 1 h. The cell proliferation was calculated using equation 5.

$$\%\ \boldsymbol{Cell\ Viability} = \left[\frac{(\boldsymbol{Fluor.Drug\ Treatment - Fluor.Blank})}{(\boldsymbol{Fluor.Control - Fluor.Blank})}\right] \times \mathbf{100} \quad \text{(Equation 5)}$$

Mean cell viability *versus* drug concentration was plotted using the Prism5 software (GraphPad Software, USA) to determine the concentration at which 50% inhibition of cell proliferation (IC_{50} value) for all test formulations. Similarly, the cell proliferation was evaluated in the 3D spheroids treated for 72 h with DTX and DTX-NLCs at concentrations ranging from 50-1000 ng/ml.

2.4.5. Cell cycle analysis

U87MG and BTNW911 cell cycle analyses were performed by propidium iodide staining. The cells were seeded and incubated at 37°C and 5% CO_2 for 24 h, followed by treatment with DTX and DTX-NLCs and incubated for further 24 h. The cells were then washed with PBS, detached with trypsin, and then the cell suspension was collected and centrifuged at 179 x g for 5 minutes. The cell pellets were resuspended and fixed by adding ice-cold 70% ethanol and stored at -20ºC for at least 24 h. The fixed cells were washed and centrifuged at 179 x g for 5 min, resuspended in PBS and placed in a V-shaped non-tissue culture 96-well plates and then treated with propidium iodide (500 µg/ml stock) followed by adding RNAase (10 mg/ml) and incubation for 2 h, prior to processing the plates using flow cytometry to determine DNA content by measuring fluorescence intensity at 488 nm for each treated population.

2.4.6. Mitochondrial Stress test

U87MG cells were seeded on a XFp culture plate and left overnight to attach and proliferate, followed by treatment with DTX and DTX-NLC for 24 h. One hour prior to assay, the cells were washed. Culture medium was replaced with XF assay medium (modified DMEM, pH 7.4 (Agilent), supplemented with glucose (25 mmol/L), glutamine 2 (mmol/L), and sodium pyruvate (2 mmol/L), and incubated at 37 °C, under CO_2 atmosphere. Oxygen consumption rate (OCR) was measured using the XFp analyser (Seahorse Bioscience). Basal OCR measurements were followed by injection of the freshly prepared XF Cell Mito Stress Test Kit (Agilent): oligomycin (1 µmol/L, injection port A), carbonyl cyanide 4-(trifluoromethoxy) phenylhydrazone (FCCP) (1 µmol/L, injection port B), and combined antimycin A

(0.5 µmol/L), and rotenone (0.5 µmol/L) (injection port C). All data were normalised to protein concentration, measured via bicinchoninic acid assay.

2.5. Statistical analysis

The statistical analysis was performed using the Kolmornov-Smirnov test for normality followed by ANOVA (with post-hoc analysis Tukey and Dunnett test) by using the Statistical Package for the Social Sciences SPSS Version 20 software (IBM Company, USA) and the Microsoft Excel software for Microsoft office 360 (Microsoft Corporation, USA). The analysis of variance was considered as statistically significant (*) when the difference $P < 0.05$ (level of confidence 95%), (**) $P < 0.01$ (level of confidence 99%), and (***) $P < 0.001$ (level of confidence 99.99%). The data are presented as the mean ± standard deviation (n=3).

3. Results

3.1. NLC optimisation and *in vitro* BBB permeability

3.1.1. Docetaxel nanostructured lipid carrier preparation and optimisation

The four NLC dispersions differed in their particle size depending upon the liquid lipid incorporated, with the smallest particle size (112.5nm) obtained with KHS15 and largest (183.6 nm) with LG90. However, all the NLCs had a fairly uniform particle size distribution as portrayed in Fig1a and Table 2. NLC B5 was developed with a combination of four liquid lipids used at lower concentrations and yielded an average particle size of 123.3 ±0.642 nm with uniform size distribution as illustrated by PDI of 0.234 ±0.016. The NLCs demonstrated a negative surface charge ranging from -32.4 ±0.967 and -26 ±0.1 mV following the order from highest to lowest ZP value B5> B1> B3> B2> B4, respectively (Table 2). The type of liquid lipid impacted the amount of drug that can be loaded onto the NLCs [15,39]. The liquid lipid has a solubilising effect on the drug and augments its incorporation in the lipid nanostructure. Liquid lipids, when used in combination (Formulation B5) resulted in the highest drug loading as compared to when each of the liquid lipids was used individually (Table 2).

3.1.2. Permeability across 3D *in-vitro* BBB model

The five NLC formulations were examined further for their permeability across the 3D *in vitro* BBB model. The acquired data for B4 and B5 NLCs demonstrated permeation of both the formulations through the

model starting from an early time point when TEER values dropped at 0.25 h, followed by continuous low TEER values up to 1 h for B4 and 2 h for B5 and a subsequent increase thereafter until the TEER returned to normal base value at 4 h and was maintained till 6 h when the experiment was terminated. TEER values reflect the tightness of the intercellular junctions and are powerful indicators of the integrity of the cellular barriers [40]. The decrease in TEER followed by its complete recovery signifies the transient and reversible opening of the tight intercellular junctions (TJs) when in contact with NLCs allowing paracellular permeation followed by restoration of the integrity of the model [41,42]. The other three formulations followed the same initial pattern of TEER value decrease as B4 and B5. However, noteworthy is the TEER values for B1, B2 and B3 formulations failed to return to baseline values, demonstrating that high concentration of individual liquid lipids incorporated in these NLCs probably led to an irreversible disruption of paracellular TJ integrity and breach of the BBB (Fig1 b) [24]. This has been evidenced in previous reports which show that the extent of decrease in TEER is a dose and concentration-dependent [43] and is determined by the concentration of excipients used in the formulation [22]. Vllasaliu *et al.* revealed that reversibility of TEER of Calu-3 cells monolayer was concentration-dependent when treated with chitosan nanoparticles [44].

Formulation B5 further referred to as DTX-NLC emerged as the most promising formulation with highest drug loading (88.6%) and ability to permeate the BBB *in-vitro* model with a Papp $2x10^{-3}$ cm/sec, without the loss of TJ integrity and was thence extensively characterised and evaluated for its potential in treating GB.

3.2. NLCs characterisation

3.2.1 Transmission electron microscopy (TEM), asymmetric Flow Field-Flow Fractionation and Nanoparticle tracking analysis (NTA)

The TEM shows spherical morphology for DTX-NLCs and B-NLCs with few oblong structures seen for B-NLCs with particle size < 200 nm (Fig1 c and d). Both radius of gyration (Rg) and hydrodynamic radius (Rh) were calculated for B-NLC and DTX-NLC (Table 3). The quantitative results from AF4-MALS-UV-DLS and batch DLS are displayed in Table 3. It is apparent that there is a difference in the Rg measured for both samples, but the Rh remains the same. The data demonstrated that the batch DLS and the online DLS measurements agree well. However, the online measurements clearly show a distribution of Rh from

~20nm to ~90nm. By contrast, the batch DLS measurement does not show this polydispersity due to the intensity bias of the technique [45]. The Rg data confirms the size distribution showing values for B-NLC from ~10nm to ~120nm and DTX-NLC from ~10nm to ~99nm (Fig1e i-iv). The ratio of Rg/Rh which represent any shape or conformation alterations in NLCs, present similar changes for both blank and drug-loaded NLCs until ~45min elution time (~50nm Rg, ~60nm Rh), beyond which B-NLCs show a higher increase in the Rg/Rh ratio (Fig1e v). Similar to DLS, NTA determines the size of particles by measuring their diffusion coefficient. The NTA data (Fig1f i and ii; video Supplementary) verified the uniform size distribution and mean particle size of DTX-NLCs as 126.7 ±0.5 nm.

3.2.2. *In-vitro* drug release

DTX being a very poorly water soluble drug, PBS pH7.4 (70%) with ethanol (30%) was used as the release medium to achieve sink conditions [37]. DTX-NLC showed a biphasic release with more than 40% of the drug being released in 2 h followed by a sustained release over 24h (Fig2 a), in contrast to its native drug suspension which elicited a release of only 40% at the end of 24h due to its low solubility [46].

3.2.3. X-ray diffractometer (XRD)

XRD pattern of all tested samples are displayed in Fig S1. The surfactant sodium cholate showed a broad peak at 2Ɵ value of 14.36 while Phospholipon 90 showed a high-intensity peak at 6.29° and medium intensity peaks at 9.5°, 12.8°, 14.4°, 16.1°, 17.7°, 19.3°, 20.2°, 21,09°, 22.2° and 23.05° respectively. The lipid Dynasan 114 demonstrated peaks of low-intensity at 35.06°, medium intensity at 7.4°, 10.2°, 15.3°, 16.6°, 17.05°, 17.6° and very high-intensity peak at 19.3°, 22.5°, 24.06°, 24.10° revealing its crystalline nature as previously stated by Severino *et al.* [47]. Moreover, DTX sample showed its usual peaks at 2Ɵ values of 5.4°, 8.1°, 10.18°, 11.4°, 12.7°, 14.2° and 17.17° in line with a previous study by Fang *et al.* [48]. In the physical mixture, the peaks of the individual components were observed at 7.4°, 16.7°, 17.3°, 17.9°, 19.4°, 23.29° and 24.14°. The DTX-NLC diffraction pattern revealed the absence of DTX peaks with lipid and surfactant peaks appearing at 2Ɵ of 7.8°, 15.05°, 15.68°,16.8°, 17.4°, 19.5°, and 24.2° confirming the amorphous nature of the entrapped drug within the NLCs.

3.2.4. Thermogravimetric analysis (TGA)

TGA revealed thermal stability of DTX with major degradation at around 204°C (6% weight loss), in line with Kulhari *et al.,* findings [49]. However, mild degradation with approximately 2% loss was observed at an initial temperature around 53°C, and 110°C (3% loss) (Fig S2). Dynasan 114 is relatively a stable lipid with 8% weight loss at 320°C. The B-NLC showed an early degradation at 204°C as compared to Dynasan 114, followed by an increase in degradation around 260°C with 10% weight loss. The DTX-NLC showed higher degradation 15% loss in comparison to the B-NLC (8% loss) at 204°C however DTX degradation at 53° and 110°C was prevented probably because of its encapsulation in NLC matrix (Fig S2).

3.2.5. Differential scanning calorimetry (DSC)

DSC thermographs for Dynasan 114 demonstrated an endothermic melting peak at 59.33°C and exothermic peak at 28.57°C, representing its recrystallisation during the cooling cycle [31]. The endothermic melting peak for DTX was observed at 170.46°C (Fig S3) [31]. Shifting of Dynasan114 was observed in the B-NLC, which exhibited a characteristic lipid melting peak at 55.61°C in the first heat cycle (Fig S3). Additionally, B-NLC exhibited lipid recrystallisation during cooling as evident from the exothermic peaks detected at 25.18°C (Fig S3). DTX-NLC showed melting peak at 54.42° C attributed to Dynasan 114, and no DTX peaks were observed demonstrating that DTX in the formulations might be in an amorphous state or the solid-solution state after encapsulation into the NLCs (Fig S3).

3.2.6. Fourier-transform infrared spectroscopy (FTIR)

FTIR of DTX demonstrated the characteristic vibrational band assignments, which are in conformation with previous reports [48]. DTX-NLC showed the characteristic peaks of DTX at positions 3688, 1700, 1457 and 1368 cm^{-1} that correlates to OH stretching, C=O stretching, N-H diffraction and C-H bending respectively (Fig 2b, Table S1). Also, the DTX-NLC had all the characteristic peaks that were present in the B-NLC ascribed to lipids and surfactants used in the formulation (Fig 2b and Table S1).

3.2.7. Raman spectroscopy

The Raman spectra of DTX and DTX-NLCs are portrayed in Fig S4, and band assignment data is given in Table S2. Peak shifts were observed at 1783, 1658, 1626, 1605, 1533, 1261, 1079, 1061, 908, and 842 cm^{-1} while other corresponding peaks of DTX were retained in DTX-NLC construing the encapsulation of DTX within the DTX-NLC.

3.2.8. Colloidal stability

DTX-NLC maintained good stability in water, as well as dextrose (5%) over a period of 24 h with no significant change in the particle size and PDI, however, in the presence of NaCl (0.9%) and PBS, a drastic increase in both particle size and PDI were observed (Fig2 c). This increase in size can be attributed to the attractive interactions between the nanoparticle surface and solute ions resulting in an ionic liquid-based supramolecular structured shell that surrounds the nanoparticles [50]. Nanoparticles are known to interact with biological fluids with the formation of the protein corona. As EMEM was used in cell culture studies, the colloidal stability of DTX-NLC was investigated in this media. A slight increase in the particle size and PDI was observed up to 6 h beyond which it remained stable (Fig2 c). This could be attributed to the adsorption of ions and/or amino acids present in the culture medium onto the surface of nanoparticles [51].

3.2.9. Short and long-term stability

Both B-NLC and DTX-NLC as aqueous dispersion maintained stability for all the investigated parameters over the period of three months. a similar concept was reported over the course of 90 days [52]. There was no change observed for the particle size and PDI (Fig3 a i and ii). with ZP maintained (> -32mV). Moreover, ~ 15 % reduction in TD was observed at the end of three months (Table 4). In terms of long-term stability, no significant increase in the particle size was observed for freeze-dried samples stored at -20°C for up to six months which was characterised with high %DL and %EE; and a slight increase in the particle size observed when DTX-NLC stored at 4°C for up to six months. DTX-NLC suffered from a significant increase in the particle size and reduction in DL when stored at 25°and 40°C at all time points, indicating that high temperature was not suitable for storing the formulation (Fig3 b and Fig S5 and S6). In addition, the DTX-NLC demonstrated good visual appearance for both freshly prepared formulation (Fig3 c) and the free-flowing powder freeze-dried form (Fig3 c) and after its reconstitution with purified water (Fig3 c). The DTX-NLC followed a trend of Oswald ripening when stored at -20, 4, 25 and 40°C (Fig3 d) as the r^2 versus time plots demonstrated a relatively linear relationship [53]. However, DTX-NLC stored at 40°C also demonstrated coalescence and flocculation (Fig3 d).

3.3. *In vitro* Cell lines studies

3.3.1. Qualitative and quantitative cellular internalisation

Visualisation of R-DTX-NLCs using confocal microscopy demonstrated the green fluorescence of R123 illustrating high internalisation inside the U87MG cells following 4 h of treatment (Fig 4a). In contrast, SVG P12 non-cancerous cells showed lower uptake as shown by less intense green colour in the cytoplasm (Fig 4b). The flow cytometer histograms shift reveals both time and concentration-dependent cell uptake for R-DTX-NLC (Fig 4c-g). Both GBs cells, U87MG and patient-derived BTNW911 short-term culture displayed an early uptake starting at 0.5 h, which continued with maximum uptake at 24 h (Fig 4c-e). In comparison, non-cancerous brain cell lines SVG P12 demonstrated lower peak intensity connoting slower cellular uptake of DTX-NLC (Fig 4c and f). In addition, the macrophages RAW 264.7 cells exhibited a lower uptake in comparison to all the other three cell lines Fig 4g. Additionally, both U87MG and SVG P12 demonstrated a dose-dependent uptake with U87MG cells showing higher uptake than SVG P12 cells (Fig 5a and b).

A spheroid illustration portrayed in Fig 5c identifies the three gradients of oxygen, metabolites and nutrients levels within in the spheroids, ensuing the central necrotic core which is surrounded by quiescent viable cells and actively proliferating peripheral cells [54]. The flow cytometer histograms (Fig 5d) delineated two distinct populations for cellular uptake of the R-DTX-NLC. The actively proliferating peripheral cells on the surface of the spheroids likely take the nanoparticles more rapidly as compared to the necrotic core or surrounding quiescent viable cells (Fig 5c). The penetration of NLCs to the core of spheroids is much slower due to their restricted passage through the extracellular matrix, which explains the presence of two peaks (Fig 5d). These results are in line with a recent report by Tchoryk *et al*. [55].

3.3.2. Mechanism of cellular uptake

The quantitative and qualitative uptake of DTX-NLCs in U87MG and SVG P12 cells was significantly less as observed by low fluorescence intensity within the cells and low MFI ($P < 0.001$) (Fig 4a and b, Fig 5e and f, Fig S7 and S8) when incubated at 4°C for 2 and 4 h as compared to 37°C (Fig 4a and b, Fig 5e and f, Fig S7). The results illustrate that the cellular uptake of NLCs is an active energy-dependent endocytosis process [56]. Nanoparticles uptake can differ in their mechanism depending upon the cell type. Our findings indicate that micropinocytosis (cytochalasin B inhibition) was the major internalisation

pathway for the DTX-NLCs in U87MG cells. However, clathrin-mediated (sucrose inhibition) and caveolae/lipid rafts (nystatin inhibition) also contributed to its uptake. In the case of SVG P12 cells, all three pathways micropinocytosis, caveolae, clathrin-mediated were equally involved in the internalisation of DTX-NLC (Fig 5e and f; Fig S7, S8). In BTNW911 cells, the participation of clathrin was primarily responsible for its uptake, followed by micropinocytosis/phagocytosis and caveolae-mediated uptake (Fig 5e and f).

3.3.3. DTX-NLCs uptake in *in-vitro* BBTB model with U87MG and BTNW911 monolayers

The R-DTX-NLC showed good permeability across the BBTB in the presence of patient-derived GB cells and U87MG as illustrated in Fig 6a, with high Papp $1x10^{-3}$ and $1.6x\ 10^{-3}$ cm/sec, respectively (Fig 6b). In the presence of DTX-NLCs TEER values dropped at 1 and 2 h of incubation followed by a gradual increase and return to normal baseline values at around 4 h. This construes transient and reversible opening of the BBTB, suggesting paracellular transport of NLCs. Following permeation through the BBTB model, a significantly higher ($P < 0.001$) uptake of DTX-NLCs was observed in BTNW911 cells as compared to U87MG (Fig6 c). These results revealed that the NLCs cross the BBTB to target and accumulate in GB cells [57].

3.3.4. Effect on Cell proliferation

DTX-NLCs showed no significant difference in IC_{50} in comparison to DTX alone at 72 h of treatment (Table 5), which suggested that DTX-NLC was as cytotoxic as native DTX towards U87MG. The DTX-NLC was less cytotoxic to normal brain SVG P12 cells (~8 times lower IC_{50}) as compared to DTX. On the other hand, DTX-NLCs showed significantly higher IC_{50} ($p < 0.001$) with BTNW911 cells at 72 h (Table 5). The short-term primary derived cultures seem more resistant to chemotherapy than U87MG cells warranting higher doses or longer treatment times. The B-NLC were found to cytocompatibility and with no cell cytotoxicity and can be safely used as a vehicle to carry the chemotherapeutic drugs. Interestingly, DTX-NLCs showed ~3.5 times higher efficacy in 3D U87MG spheroids as compared to DTX with a reduction in the spheroid diameter at higher concentration of DTX-NLC (Table 5 and Fig 7a).

3.3.5 Cell cycle analysis

Following 24 h treatment of U87MG and BTNW911 cells with DTX-NLC and DTX, a significant increase in G2/M phase, which taxanes are widely known to display [58], was observed as compared to the untreated cells as a control. The percentage of cells in G2/M phase escalated to 85.05% (U87MG) and 68.69% (BTNW911) in the DTX-NLCs group from 28.54 and 42.69 %, respectively in the control group (Fig 7b and c).

3.3.6. Mitochondrial Stress test

DTX-NLC significantly ($P<0.01$) inhibited the mitochondrial oxygen consumption rate (OCR) and cellular respiration in U87MG cells. The OCR rate of DTX-NLC reduced to 0.44±0.05 pmol/min/protein as compared to 2.72±0.30 pmol/min/protein of control cells. However, native DTX did not show any significant reduction in OCR rate (2.58±0.31 pmol/min/protein) (Fig 8a and b). Similarly, a significant reduction in extracellular acidification rate (ECAR) of DTX-NLC (0.57±0.28 mpH/min/protein) was observed as compared to control (1.47±0.73 mpH/min/protein) and DTX (1.45 ± 0.72 mpH/min/protein) (Fig 8c) signifying that there was significant suppression of basal OCR, ATP-linked OCR, and maximal uncoupled OCR on treatment with DTX-NLC (Fig 8a-c) [59].

4. Discussion

NLCs the second-generation lipid nanoparticles have received much attention in the last two decades to deliver drugs across various biological barriers. NLCs have been investigated for brain delivery because of its lipophilicity [60]. However, many studies attach ligands like transferrin to improve their brain targeting [61,62]. The present study utilised the inherent properties of liquid lipids to facilitate the NLCs permeation across BBB and BBTB. Furthermore, the solubilising effect of liquid lipids was exploited to load higher quantities of very poorly soluble drug DTX. For brain permeation, it is vital that the agents which enhance permeability across the BBB should be safe and retain the barrier function of BBB. NLCs fabricated with each of the four liquid lipids (LG90, CPGMC, LB and K HS15) showed good permeation across the *in vitro* BBB model as demonstrated by the Papp values. KHS15 have previously shown to enhance BBB permeability probably due to inhibition of efflux pump P-gp expressed on BBB endothelial cells known to efflux drugs and small molecules [63]. LG90, CPGMC, LB are known for their permeation enhancement through skin barrier [28]. Previous studies have also shown LB as a substrate of efflux

transporter P-gp and shown good transport across Caco-2 intestinal permeability model [64]. This is the first report of studies on brain permeability with these compounds.

NLCs with high concentrations of LG90, CPGMC and LB were found to affect the integrity of BBB as was discerned from poor recovery of TEER to the base value and EBD leak as demonstrated by high EBD concentration in the basal side the BBB model at the end of the experiment [24]. Previous study has shown partial recovery or irreversible disruption of Caco-2 cell monolayers when treated with high concentrations of LB and LG90 used as co-processed excipients [22]. TEER values are strong indicators of the integrity of cellular barriers [36]. Transient reduction of TEER values and returning to normal base value represent a reversible opening of TJs and paracellular transport [39,41]. TJs of endothelial cells are complex structures composed of integral membrane proteins, linker proteins connecting membrane proteins to the actin cytoskeleton and signalling molecules regulating paracellular tightness and transport. Transmembrane TJ proteins occludin and the members of the claudin family play a prominent role in forming paracellular barriers along with adherens junctions composed of VE-cadherin protein which mediate cell to cell adhesion and maintain biophysical stability of the barrier [36,65]. Failure of TEER to return to the original values indicate a disruption of junctional proteins affecting TJ integrity [65] resulting in impaired endothelial barrier function. Shubber *et al.* have shown altered F-actin morphology at the high concentration of KHS15 and lower recovery of TEER values relative to baseline values, while full recovery of TEER values when the excipient was used in lower concentrations in a Calu-3 model [22]. Similar finding have been reported by Vllasaliu *et al*. with complete recovery of TEER at low concentration and no recovery at high concentration of chitosan nanoparticles [44]. Thus, tailoring the concentration of excipients to modulate the permeability of NLCs with the reversible opening of TJ without membrane disruption is important for optimisation of the formulation for drug delivery across BBB. The rationalised approach of using a combination of four liquid lipids at five times lower concentration in formulation B5 permitted paracellular transport of NLCs across BBB with the opening of TJs between 0.25 -2 h of treatment but without alteration in the integrity of TJ which was amply demonstrated by a complete recovery of TEER at 4h and no EBD leak in the donor compartment at the end of the experiment at 6h. B5 indicated a high BBB permeation as compared to previously reported formulations intended for brain delivery due to its high Papp value

[66]. Adopting a combination of liquid lipids approach in the design of NLCs also had a positive impact on DL and high DTX loading of 88.6% could be achieved which is higher than other NLCs prepared with single liquid lipid. Optimisation of solid and liquid lipid blends and the impact of liquid lipid on functional properties of NLCs is well recognised in previous reports [15,67]. This optimised formulation was successfully freeze-dried with10% Trehalose as cryoprotectant and was extensively characterised.

The size and ZP of nanomaterials play important roles in their fate *in vivo*. The DTX-NLCs exhibited a fairly uniform particle size as testified by low PDI values 0.234±0.16 [31], and a ZP of -32.4 ±0.967 predicting good stability [68,69]. The mean particle size obtained from DLS and NTA were in confirmation with each other [70] and well in agreement with previous reports utilising NPs for brain delivery [71]. AF4 data construed that incorporation of DTX increased the core density and resulted in lower particle size (40nm radius) than the equivalent B-NLCs without the drug. The DTX-NLCs exhibit spherical structure irrespective of the size of nanoparticles as illustrated by uniform Rg/Rh ratios and confirmed by TEM. However, the B-NLCs exhibited elongated structures for the particles of larger sizes (above Rg 50nm, Rh 60nm) present in the sample apparently due to lack of dense core which is also confirmed by the TEM images which show few oblong structures of larger particle size [72].

DTX-NLC released more than 40% of drug at 2 h, presenting a biphasic profile with the initial burst release followed by a slow, sustained release, which is in line with a previous report [73]. This is possibly due to the fast diffusion of solubilised DTX molecules on the surface of the DTX-NLCs, followed by slow release of molecules present in the core [74]. A sustained-release effect is more favourable than faster drug release, particularly for intravenous administration [75]. The XRD structure of the DTX-NLC indicated DTX likely present in an amorphous state within the NLCs since the characteristic peaks of DTX were absent. This was in confirmation with the DSC data, demonstrating that DTX is presumably in an amorphous state or the solid-solution state after encapsulation into the NLCs [31]. FTIR and Raman spectroscopy established the presence of DTX within the DTX-NLC due to appearance of characteristic DTX peak in the DTX-NLC spectra [76]. TGA revealed major degradation of DTX at higher temperatures even with a very stable solid lipid Dyanasan 114, emphasising the importance of controlling the temperature during the processing of DTX-NLC.

Since DTX-NLC is intended for intravenous administration to treat cancer, it is imperative to study its colloidal stability in the presence of various physiological solutions. The colloidal stability is reflected by changes in the particle size and distribution and it is a critical element to predict the stability and fate of the nanoparticles for the *in vitro* and *in vivo* intended use. Dextrose 5% and water maintained colloidal stability of DTX-NLC since the particle size and PDI were not affected following 24 h incubation [77]. While DTX-NLC showed a sharp increase in the particle size and PDI in NaCl 0.9% and PBS, leading to aggregation of the particles. The poor stability is attributed to the presence of anionic moieties in these salt solutions causing a change in the surface charge of DTX-NLC and consequently leading to aggregation or due to potential formation of insoluble salts of drug that might lead to precipitation from the colloidal dispersion and co-precipitate colloidal particles along with it [77]. NLCs dispersed in EMEM media should be preferably used within 6 h, beyond which appreciable increase in the particle size and PDI were observed. Proteins and vitamins present in the EMEM media presumably adsorb onto the NPs surface with formation of a corona resulting in an increase in the particle size [78]. Therefore, water or dextrose 5% would be good media for reconstitution of freeze-dried NLCs and an anionic physiological solution would be best avoided to avert any particle aggregation.

DTX-NLC and B-NLC dispersions showed good storage stability due to high ZP > -30 mV, which was maintained over a period of three months [79]. High ZP plays a crucial role to prevent particle aggregation, as the electrostatic repulsion prevents aggregation of particles leading to good colloidal stability [69]. The drug content of NLCs was reduced by ~20% due to the labile nature of DTX. Lyophilisation of the formulation results in better long term stability of DTX-NLC and with no drug loss when stored at -20°C and % EE and % DL were maintained for up to six months. Also, no significant increase in the particle size was observed. On the other hand, DTX-NLC stored at 4°C showed an increase in the particle size (230 nm) after 6 months of storage. DTX-NLC stored at 25 ^{0}C and 40°C showed significant increase in the particle size to ~230nm and ~460nm respectively attributed to Ostwald's ripening as demonstrated by relatively linear r^2 vs time plots [53]. This phenomenon occurs as small particle accumulate and dispose into larger particles. DTX-NLC stored at 40°C also demonstrated coalescence and flocculation in addition to Ostwald's ripening.

Cell culture studies were aimed at understanding the internalisation mechanism of NLCs in the GB cells and if it differs from non-cancerous cells. The qualitative data by confocal microscopy illustrated the co-localisation of NLCs and exhibited their accumulation in the cytoplasm of cells, while the quantitative analysis revealed that the internalisation of DTX-NLCs increased with time and dose. However, the extent of internalisation differed depending upon the type of the cells. A notable lower uptake was exhibited by the SVG P12 cells, indicating the safety of the DTX-NLC towards non-cancerous brain cell. Encapsulation of therapeutic agents in lipid nanoparticles has been previously reported to reduce its toxicity to normal cells [80]. Interestingly, the BTNW911 short-term culture showed significantly higher uptake in comparison with U87MG cell lines, indicating a more relevant data since it was derived from patients. In addition, the low uptake by the macrophage cells RAW 264.7 is beneficial proposedly allowing longer circulation in the bloodstream and avoidance of opsonisation and rapid clearance by the mononuclear phagocytic system [81].

Furthermore, since 3D models are more reliable and relevant tools for evaluating in a relatively realistic environment than 2D models [82]; DTX-NLCs were examined in 3D U87MG spheroids to understand their tumour penetration. The DTX-NLCs readily penetrated the actively proliferating peripheral cells through the penetration in the necrotic core was more delayed taking longer time for penetration [54].

DTX-NLCs were taken up by energy-dependent endocytosis process in U87MG, SVG P12 and BTNW911 cells though the predominant mechanism pathways differed with the cell type [83]. Micropinocytosis/phagocytosis involving actin filaments to internalise particles was the major pathway in SVG P12 and U87MG cells. In addition, both cell lines showed a disruption of the uptake process when the cells were incubated under a hypertonic environment, suggesting that the NLCs were internalised through the clathrin-mediated pathway, though this pathway was more predominant in the SVG P12 cells [84]. Involvement of caveolae was also exhibited as revealed by nystatin disruption of lipid rafts in the cell membrane inhibiting entry of NLCs in SVG P12 and U87MG cells [85]. For BTNW cells, clathrin-mediated was the more dominant pathway, followed by micropinocytosis and caveolae-mediated pathway. Interestingly, all the three pathways, clathrin-, caveolae- and micropinocytosis, contributed to the internalisation of the NLCs. This corroborates with previous reports where lipid nanoparticles have shown to be internalised by more than one pathways [86].

The BBTB model was built to simulate the environment at an early stage of GB, whereby the GB can induce changes in the permeability of BBB. BBTB/U87MG and BBTB/BTNW both models were investigated. The TEER values of BBTB model increased to ~300 (Ω/cm^2) exhibiting the BBTB remain intact, and the presence of GB cells did not affect the integrity of the model. On treatment with DTX-NLCs, the TEER dropped at 0.25h but gradually built back with complete recovery at 6 h. DTX-NLCs reversibly open the TJs for paracellular transport. Shubber *et al.* have reported permeability enhancement and the consequent impact on cell cytoskeleton in terms of actin organization and tight junction opening of Calu-3 cell monolayers along with increased endocytosis rate in the presence of Kolliphor® HS15 [87]. Similarly, LB and LG have shown increased permeation and opening of TJs of Caco-2 cells with altered distribution of claudin-1 transmembrane protein responsible for paracellular transport [22,88]. Their increase in permeability has also been attributed to their ability to insert themselves between the plasma membrane lipid tails of the lipid bilayer and fluidise the membrane [24]. Lipidic nature of NLCs promotes their uptake through low-density lipoprotein receptors expressed predominantly on the BBB [89]. GBs cells exhibit overexpression of vascular endothelial growth factor (VEGF), which is an angiogenesis factor. VEGF might be related to the increase in the permeability of the BBTB model [90]. Furthermore, LB and KHS15 also cause P-gp efflux pump inhibition which also aids in permeation through the BBTB model [91,92]. Thus paracellular diffusion and receptor-mediated endocytosis both mechanisms would lead to enhanced BBB/BTB crossing of DTX-NLCs [93]. Following permeability through the BBTB model, DTX-NLCs were readily uptaken by the GB cells. BTNW911 uptake was ~ 2.4 folds higher than U87MG cells. The data obtained through screening formulation via BBTB were more relevant since it was tested through an all human brain model and glioma patient-derived short term culture [30,94].

DTX-NLCs showed an equal efficacy as native DTX towards U87MG since no significant difference in IC_{50} at 72 h was observed. In addition, our data suggested a time-dependent delay to reach this equivalent effect, that might be attributed to the slow release of DTX from DTX-NLC as previously reported by Koopaei *et al.* [74]. BTNW911 showed more resistance to DTX-NLCs as observed with a significant increase in the IC_{50} after 72 h of treatment. Though cells grown in 3D tumour models are more resistant to chemotherapy drugs [95] notably, DTX-NLC indicated a superior effect (significantly low IC_{50}) than DTX native drug that indicated a more relevant data since cells grown in 3D models are more resemblance to *in*

vivo than monolayer cell lines. DTX is a well-known mitotic inhibitor, and it can suppress cell growth by inducing G2/M cell cycle arrest [96]. It is worth noting that DTX-NLC showed a higher percentage of cells in G2/M cell phase in comparison to native DTX as well as control cells in both the tested cell lines. Noticeable and significant effect of DTX-NLC, but not DTX, on mitochondrial respiration is interesting, given that we saw no difference in cytotoxicity between the two groups. This suggests DTX-NLCs apparently has a mitochondrial-specific effect, not seen with native DTX. The reason behind this DTX-NLC-specific effect on mitochondria is unknown. Still, it may be explained by the early-stage initiation of the apoptotic process and certainly requires further work to investigate the temporal and mechanical aspects of this observation. Moreover, DTX-NLC caused a decrease in the mitochondrial reserve capacity of cells, indicating that the lipid carrier increased the ability of the drug to impair oxygen consumption and thus the cells' ATP-producing capability [97]. The lipid nanocarrier increased the drug's effect on cell viability by inducing arrest and impairing mitochondrial aerobic metabolism, which is an increasingly crucial therapeutic target in cancer drug discovery [98,99]. Thus NLCs present as one of the most promising carriers for treating cancer [100].

3. Conclusion

As the presence of the BBB will persist in being an obstacle for all CNS treatment, the research for an optimum drug delivery strategy to deliver drugs across this formidable barrier will continue. A novel approach of using a rational combination of four liquid lipids at low concentrations in an NLC formulation has been used to enhance the permeation of a CNS negative drug DTX across the BBB and BBTB to deliver the chemotherapeutic drug to GB cells without disrupting the barrier properties in a 3D *in-vitro* model. The formulation produced using a simple and scalable melt emulsification process to form DTX-NLCs, which exhibited low particle size (123 nm), uniform distribution (PDI 0.23) and spherical shape with desirable surface charge (ZP -32 mV) and high drug entrapment (99%) and maintained stability for six months in the freeze-dried form. DTX-NLC preserved its colloidal stability in water and dextrose 5% up to 24h and could be a useful media for reconstitution of the freeze-dried formulation. XRD, DSC, FTIR and Raman spectrums confirmed the encapsulation of DTX and its presence in an amorphous state in the NLC matrix. The NLCs showed higher internalisation by GB cells (U87MG) and patient-derived short-term primary culture (BTNW911) over the non-cancerous brain cells (SVG P12) and macrophages (RAW

264.7) with preferred ability to penetrate 3D U87MG spheroids. DTX-NLC effectively inhibited both GB cells, U87MG and BTNW911 with low IC_{50} at 72 h of treatment inducing cell arrest via G2/M phase with a distinctive decrease in the mitochondrial reserve capacity of cells. The present study opens the door for a simple yet effective strategy for GB targeting and further options of its application to enhance BBB penetration for wider CNS therapeutics.

Acknowledgement

T Zwain acknowledges the financial support from Dr Akeel Zwain (Zwain Cardiology Clinic, Iraq). Authors thank the financial support provided by the UCLan Research Centre for Translational Biosciences and Behaviour and UCLan Research Centre for Smart Materials, University of Central Lancashire. CREMER OLEO, Germany; Lipoid, Germany and Gattefoss´e, France are gratefully acknowledged for the gift samples of the excipients. The authors thank Professor Timothy Dawson and Katherine Ashton from the Brain Tumour North West (BTNW), UK for providing the patient-derived short-term culture. Postnova Analytics UK is acknowledged for the AF4-MALS-DLS measurements and analysis.

References

[1] J.R. Hands, K.M. Dorling, P. Abel, K.M. Ashton, A. Brodbelt, C. Davis, T. Dawson, M.D. Jenkinson, R.W. Lea, C. Walker, M.J. Baker, Attenuated Total Reflection Fourier Transform Infrared (ATR-FTIR) spectral discrimination of brain tumour severity from serum samples, J. Biophotonics. (2014). https://doi.org/10.1002/jbio.201300149.

[2] Q.T. Ostrom, H. Gittleman, J. Fulop, M. Liu, R. Blanda, C. Kromer, Y. Wolinsky, C. Kruchko, J.S. Barnholtz-Sloan, CBTRUS Statistical Report: Primary Brain and Central Nervous System Tumors Diagnosed in the United States in 2008-2012, Neuro. Oncol. 17 (2015) iv1–iv62. https://doi.org/10.1093/neuonc/nov189.

[3] A.H.M. Vries Schultink, M.B.S. Crombag, E. Werkhoven, H. Otten, A.M. Bergman, J.H.M. Schellens, A.D.R. Huitema, J.H. Beijnen, Neutropenia and docetaxel exposure in metastatic castration-resistant prostate cancer patients: A meta-analysis and evaluation of a clinical cohort, Cancer Med. 8 (2019) 1406–1415. https://doi.org/10.1002/cam4.2003.

[4] V. Kushwah, S.S. Katiyar, C.P. Dora, A. Kumar Agrawal, D.A. Lamprou, R.C. Gupta, S. Jain, Co-delivery of docetaxel and gemcitabine by anacardic acid modified self-assembled albumin nanoparticles for effective breast cancer management, Acta Biomater. 73 (2018) 424–436. https://doi.org/10.1016/j.actbio.2018.03.057.

[5] N.J.S. Fauzee, Z. Dong, Y.L. Wang, Taxanes: Promising anti-cancer drugs, Asian Pacific J. Cancer Prev. 12(4) (2011) 837–51.

[6] P. Sampath, L.D. Rhines, F. DiMeco, B.M. Tyler, M.C. Park, H. Brem, Interstitial Docetaxel (Taxotere), Carmustine and Combined Interstitial Therapy: a Novel Treatment for Experimental Malignant Glioma, J. Neurooncol. 80 (2006) 9–17. https://doi.org/10.1007/s11060-006-9159-4.

[7] W. Löscher, H. Potschka, Role of drug efflux transporters in the brain for drug disposition and treatment of brain diseases, Prog. Neurobiol. 76 (2005) 22–76. https://doi.org/10.1016/j.pneurobio.2005.04.006.

[8] D. Wang, C. Wang, L. Wang, Y. Chen, A comprehensive review in improving delivery of small-molecule chemotherapeutic agents overcoming the blood-brain/brain tumor barriers for

glioblastoma treatment, Drug Deliv. 26 (2019) 551–565. https://doi.org/10.1080/10717544.2019.1616235.

[9] O. Van Tellingen, B. Yetkin-Arik, M.C. De Gooijer, P. Wesseling, T. Wurdinger, H.E. De Vries, Overcoming the blood-brain tumor barrier for effective glioblastoma treatment, Drug Resist. Updat. 19 (2015) 1–12. https://doi.org/10.1016/j.drup.2015.02.002.

[10] C.D. Arvanitis, G.B. Ferraro, R.K. Jain, The blood–brain barrier and blood–tumour barrier in brain tumours and metastases, Nat. Rev. Cancer. 20 (2020) 26–41. https://doi.org/10.1038/s41568-019-0205-x.

[11] C. Tapeinos, M. Battaglini, G. Ciofani, Advances in the design of solid lipid nanoparticles and nanostructured lipid carriers for targeting brain diseases, J. Control. Release. (2017). https://doi.org/10.1016/j.jconrel.2017.08.033.

[12] R.H. Müller, M. Radtke, S.A. Wissing, Solid lipid nanoparticles (SLN) and nanostructured lipid carriers (NLC) in cosmetic and dermatological preparations, in: Adv. Drug Deliv. Rev., 2002. https://doi.org/10.1016/S0169-409X(02)00118-7.

[13] A. Gordillo-Galeano, C.E. Mora-Huertas, Solid lipid nanoparticles and nanostructured lipid carriers: A review emphasizing on particle structure and drug release, Eur. J. Pharm. Biopharm. (2018). https://doi.org/10.1016/j.ejpb.2018.10.017.

[14] J. Pardeike, S. Weber, N. Matsko, A. Zimmer, Formation of a physical stable delivery system by simply autoclaving nanostructured lipid carriers (NLC), Int. J. Pharm. 439 (2012) 22–27. https://doi.org/10.1016/j.ijpharm.2012.09.018.

[15] C. Houacine, D. Adams, K.K. Singh, Impact of liquid lipid on development and stability of trimyristin nanostructured lipid carriers for oral delivery of resveratrol, J. Mol. Liq. 316 (2020) 113734. https://doi.org/10.1016/j.molliq.2020.113734.

[16] C.Y. Zhuang, N. Li, M. Wang, X.N. Zhang, W.S. Pan, J.J. Peng, Y.S. Pan, X. Tang, Preparation and characterization of vinpocetine loaded nanostructured lipid carriers (NLC) for improved oral bioavailability, Int. J. Pharm. (2010). https://doi.org/10.1016/j.ijpharm.2010.05.005.

[17] S. Ali, K. Kolter, Kolliphor® HS 15 - An enabler for parenteral and oral formulations, Am.

Pharm. Rev. (2019).

[18] W. Lim, P.S. RAJINIKANTH, C. Mallikarjun, Y.B. KANG, Formulation and delivery of itraconazole to the brain using a nanolipid carrier system, Int. J. Nanomedicine. (2014) 2117. https://doi.org/10.2147/IJN.S57565.

[19] W. Du, H. Li, B. Tian, S. Sai, Y. Gao, T. Lan, Y. Meng, C. Ding, Development of nose-to-brain delivery of ketoconazole by nanostructured lipid carriers against cryptococcal meningoencephalitis in mice, Colloids Surfaces B Biointerfaces. 183 (2019) 110446. https://doi.org/10.1016/j.colsurfb.2019.110446.

[20] Y. Chen, L. Liu, Modern methods for delivery of drugs across the blood–brain barrier, Adv. Drug Deliv. Rev. 64 (2012) 640–665. https://doi.org/10.1016/j.addr.2011.11.010.

[21] J.S. Coon, W. Knudson, K. Clodfelter, B. Lu, R.S. Weinstein, Solutol HS 15, nontoxic polyoxyethylene esters of 12-hydroxystearic acid, reverses multidrug resistance., Cancer Res. 51 (1991) 897–902. http://www.ncbi.nlm.nih.gov/pubmed/1988130.

[22] M.M. Alvi, P. Chatterjee, A Prospective Analysis of Co-Processed Non-Ionic Surfactants in Enhancing Permeability of a Model Hydrophilic Drug, AAPS PharmSciTech. 15 (2014) 339–353. https://doi.org/10.1208/s12249-013-0065-8.

[23] N.F. Younes, S.A. Abdel-Halim, A.I. Elassasy, Solutol HS15 based binary mixed micelles with penetration enhancers for augmented corneal delivery of sertaconazole nitrate: optimization, in vitro , ex vivo and in vivo characterization, Drug Deliv. 25 (2018) 1706–1717. https://doi.org/10.1080/10717544.2018.1497107.

[24] Y. Lo, Relationships between the hydrophilic–lipophilic balance values of pharmaceutical excipients and their multidrug resistance modulating effect in Caco-2 cells and rat intestines, J. Control. Release. 90 (2003) 37–48. https://doi.org/10.1016/S0168-3659(03)00163-9.

[25] T.B. Devkar, A.R. Tekade, K.R. Khandelwal, Surface engineered nanostructured lipid carriers for efficient nose to brain delivery of ondansetron HCl using Delonix regia gum as a natural mucoadhesive polymer, Colloids Surfaces B Biointerfaces. 122 (2014) 143–150. https://doi.org/10.1016/j.colsurfb.2014.06.037.

[26] Y.-M. Yin, F.-D. Cui, C.-F. Mu, M.-K. Choi, J.S. Kim, S.-J. Chung, C.-K. Shim, D.-D. Kim,

Docetaxel microemulsion for enhanced oral bioavailability: Preparation and in vitro and in vivo evaluation, J. Control. Release. 140 (2009) 86–94. https://doi.org/10.1016/j.jconrel.2009.08.015.

[27] L.H. Salem, G.S. El-Feky, R.H. Fahmy, O.N. El Gazayerly, A. Abdelbary, Coated Lipidic Nanoparticles as a New Strategy for Enhancing Nose-to-Brain Delivery of a Hydrophilic Drug Molecule, J. Pharm. Sci. 109 (2020) 2237–2251. https://doi.org/10.1016/j.xphs.2020.04.007.

[28] C.W. Cho, S.C. Shin, Enhanced controlled transdermal delivery of mexazolam using ethylene-vinyl acetate, Iran. J. Pharm. Res. 11(1) (2012) 3–12. https://doi.org/10.22037/ijpr.2011.1055.

[29] S. Kumar, L. Shaw, C. Lawrence, R. Lea, J. Alder, P50 * DEVELOPING A PHYSIOLOGICALLY RELEVANT BLOOD BRAIN BARRIER MODEL FOR THE STUDY OF DRUG DISPOSITION IN GLIOMA, Neuro. Oncol. 16 (2014) vi8–vi8. https://doi.org/10.1093/neuonc/nou249.38.

[30] C.L. Esposito, S. Nuzzo, S.A. Kumar, A. Rienzo, C.L. Lawrence, R. Pallini, L. Shaw, J.E. Alder, L. Ricci-Vitiani, S. Catuogno, V. de Franciscis, A combined microRNA-based targeted therapeutic approach to eradicate glioblastoma stem-like cells, J. Control. Release. 238 (2016) 43–57. https://doi.org/10.1016/j.jconrel.2016.07.032.

[31] Y.W. Naguib, B.L. Rodriguez, X. Li, S.D. Hursting, R.O. Williams, Z. Cui, Solid Lipid Nanoparticle Formulations of Docetaxel Prepared with High Melting Point Triglycerides: In Vitro and in Vivo Evaluation, Mol. Pharm. 11 (2014) 1239–1249. https://doi.org/10.1021/mp4006968.

[32] S. Kumar, J.K. Randhawa, High melting lipid based approach for drug delivery: Solid lipid nanoparticles, Mater. Sci. Eng. C. 33 (2013) 1842–1852. https://doi.org/10.1016/j.msec.2013.01.037.

[33] R.K. Mishra, A. Ahmad, A. Kumar, A. Vyawahare, S.S. Raza, R. Khan, Lipid-based nanocarrier-mediated targeted delivery of celecoxib attenuate severity of ulcerative colitis, Mater. Sci. Eng. C. (2020). https://doi.org/10.1016/j.msec.2020.111103.

[34] T. Gong, P. Zhang, C. Deng, Y. Xiao, T. Gong, Z. Zhang, An effective and safe treatment strategy for rheumatoid arthritis based on human serum albumin and Kolliphor ® HS 15,

Nanomedicine. 14 (2019) 2169–2187. https://doi.org/10.2217/nnm-2019-0110.

[35] T. Garanti, A. Stasik, A.J. Burrow, M.A. Alhnan, K.W. Wan, Anti-glioma activity and the mechanism of cellular uptake of asiatic acid-loaded solid lipid nanoparticles, Int. J. Pharm. (2016). https://doi.org/10.1016/j.ijpharm.2016.01.018.

[36] B. Srinivasan, A.R. Kolli, M.B. Esch, H.E. Abaci, M.L. Shuler, J.J. Hickman, TEER Measurement Techniques for In Vitro Barrier Model Systems, J. Lab. Autom. 20 (2015) 107–126. https://doi.org/10.1177/2211068214561025.

[37] S. Zhang, J. Guan, M. Sun, D. Zhang, H. Zhang, B. Sun, W. Guo, B. Lin, Y. Wang, Z. He, C. Luo, J. Sun, Self-delivering prodrug-nanoassemblies fabricated by disulfide bond bridged oleate prodrug of docetaxel for breast cancer therapy, Drug Deliv. (2017). https://doi.org/10.1080/10717544.2017.1381201.

[38] B. Sun, C. Luo, L. Li, M. Wang, Y. Du, D. Di, D. Zhang, G. Ren, X. Pan, Q. Fu, J. Sun, Z. He, Core-matched encapsulation of an oleate prodrug into nanostructured lipid carriers with high drug loading capability to facilitate the oral delivery of docetaxel, Colloids Surfaces B Biointerfaces. 143 (2016) 47–55. https://doi.org/10.1016/j.colsurfb.2016.02.065.

[39] N.E. Eleraky, M.M. Omar, H.A. Mahmoud, H.A. Abou-taleb, Nanostructured Lipid Carriers to Mediate Brain Delivery of Temazepam : Design and In Vivo Study, Pharmaceutics. 12(5) (2020) 451.

[40] L.-F. Blume, M. Denker, F. Gieseler, T. Kunze, Temperature corrected transepithelial electrical resistance (TEER) measurement to quantify rapid changes in paracellular permeability., Pharmazie. 65 (2010) 19–24. https://doi.org/10.1691/ph.2010.9665.

[41] A. Bocsik, F.R. Walter, A. Gyebrovszki, L. Fülöp, I. Blasig, S. Dabrowski, F. Ötvös, A. Tóth, G. Rákhely, S. Veszelka, M. Vastag, P. Szabó-Révész, M.A. Deli, Reversible Opening of Intercellular Junctions of Intestinal Epithelial and Brain Endothelial Cells With Tight Junction Modulator Peptides, J. Pharm. Sci. 105 (2016) 754–765. https://doi.org/10.1016/j.xphs.2015.11.018.

[42] C. Pucci, D. De Pasquale, A. Marino, C. Martinelli, S. Lauciello, G. Ciofani, Hybrid Magnetic Nanovectors Promote Selective Glioblastoma Cell Death through a Combined Effect of

Lysosomal Membrane Permeabilization and Chemotherapy, ACS Appl. Mater. Interfaces. 12 (2020) 29037–29055. https://doi.org/10.1021/acsami.0c05556.

[43] A. Taverner, R. Dondi, K. Almansour, F. Laurent, S.-E. Owens, I.M. Eggleston, N. Fotaki, R.J. Mrsny, Enhanced paracellular transport of insulin can be achieved via transient induction of myosin light chain phosphorylation, J. Control. Release. 210 (2015) 189–197. https://doi.org/10.1016/j.jconrel.2015.05.270.

[44] D. Vllasaliu, R. Exposito-Harris, A. Heras, L. Casettari, M. Garnett, L. Illum, S. Stolnik, Tight junction modulation by chitosan nanoparticles: Comparison with chitosan solution, Int. J. Pharm. (2010). https://doi.org/10.1016/j.ijpharm.2010.08.020.

[45] F. Caputo, A. Arnould, M. Bacia, W.L. Ling, E. Rustique, I. Texier, A.P. Mello, A.-C. Couffin, Measuring Particle Size Distribution by Asymmetric Flow Field Flow Fractionation: A Powerful Method for the Preclinical Characterization of Lipid-Based Nanoparticles, Mol. Pharm. 16 (2019) 756–767. https://doi.org/10.1021/acs.molpharmaceut.8b01033.

[46] S. Akhtartavan, M. Karimi, K. Karimian, N. Azarpira, M. Khatami, H. Heli, Evaluation of a self-nanoemulsifying docetaxel delivery system, Biomed. Pharmacother. (2019). https://doi.org/10.1016/j.biopha.2018.11.110.

[47] P. Severino, S.C. Pinho, E.B. Souto, M.H.A. Santana, Crystallinity of Dynasan®114 and Dynasan®118 matrices for the production of stable Miglyol®-loaded nanoparticles, J. Therm. Anal. Calorim. 108 (2012) 101–108. https://doi.org/10.1007/s10973-011-1613-7.

[48] G. Fang, B. Tang, Z. Liu, J. Gou, Y. Zhang, H. Xu, X. Tang, Novel hydrophobin-coated docetaxel nanoparticles for intravenous delivery: In vitro characteristics and in vivo performance, Eur. J. Pharm. Sci. 60 (2014) 1–9. https://doi.org/10.1016/j.ejps.2014.04.016.

[49] H. Kulhari, D.P. Kulhari, M.K. Singh, R. Sistla, Colloidal stability and physicochemical characterization of bombesin conjugated biodegradable nanoparticles, Colloids Surfaces A Physicochem. Eng. Asp. 443 (2014) 459–466. https://doi.org/10.1016/j.colsurfa.2013.12.011.

[50] Z. He, P. Alexandridis, Nanoparticles in ionic liquids: interactions and organization, Phys. Chem. Chem. Phys. 17 (2015) 18238–18261. https://doi.org/10.1039/C5CP01620G.

[51] T.L. Moore, D.A. Urban, L. Rodriguez-Lorenzo, A. Milosevic, F. Crippa, M. Spuch-Calvar, S.

Balog, B. Rothen-Rutishauser, M. Lattuada, A. Petri-Fink, Nanoparticle administration method in cell culture alters particle-cell interaction, Sci. Rep. 9 (2019) 900. https://doi.org/10.1038/s41598-018-36954-4.

[52] J.A. Oshiro-Junior, M.R. Sato, F.I. Boni, K.L.M. Santos, K.T. de Oliveira, L.M. de Freitas, C.R. Fontana, D. Nicholas, A. McHale, J.F. Callan, M. Chorilli, Phthalocyanine-loaded nanostructured lipid carriers functionalized with folic acid for photodynamic therapy, Mater. Sci. Eng. C. (2020). https://doi.org/10.1016/j.msec.2019.110462.

[53] P. Witayaudom, U. Klinkesorn, Effect of surfactant concentration and solidification temperature on the characteristics and stability of nanostructured lipid carrier (NLC) prepared from rambutan (Nephelium lappaceum L.) kernel fat, J. Colloid Interface Sci. 505 (2017) 1082–1092. https://doi.org/10.1016/j.jcis.2017.07.008.

[54] G. Mehta, A.Y. Hsiao, M. Ingram, G.D. Luker, S. Takayama, Opportunities and challenges for use of tumor spheroids as models to test drug delivery and efficacy, J. Control. Release. 164 (2012) 192–204. https://doi.org/10.1016/j.jconrel.2012.04.045.

[55] A. Tchoryk, V. Taresco, R.H. Argent, M. Ashford, P.R. Gellert, S. Stolnik, A. Grabowska, M.C. Garnett, Penetration and Uptake of Nanoparticles in 3D Tumor Spheroids, Bioconjug. Chem. 30 (2019) 1371–1384. https://doi.org/10.1021/acs.bioconjchem.9b00136.

[56] A. Akbari, A. Lavasanifar, J. Wu, Interaction of cruciferin-based nanoparticles with Caco-2 cells and Caco-2/HT29-MTX co-cultures, Acta Biomater. 64 (2017) 249–258. https://doi.org/10.1016/j.actbio.2017.10.017.

[57] H. Ruan, X. Chen, C. Xie, B. Li, M. Ying, Y. Liu, M. Zhang, X. Zhang, C. Zhan, W. Lu, W. Lu, Stapled RGD Peptide Enables Glioma-Targeted Drug Delivery by Overcoming Multiple Barriers, ACS Appl. Mater. Interfaces. 9 (2017) 17745–17756. https://doi.org/10.1021/acsami.7b03682.

[58] M.C.O. da Rocha, P.B. da Silva, M.A. Radicchi, B.Y.G. Andrade, J.V. de Oliveira, T. Venus, C. Merker, I. Estrela-Lopis, J.P.F. Longo, S.N. Báo, Docetaxel-loaded solid lipid nanoparticles prevent tumor growth and lung metastasis of 4T1 murine mammary carcinoma cells, J. Nanobiotechnology. 18 (2020) 43. https://doi.org/10.1186/s12951-020-00604-7.

[59] P. Navarro, M.J. Bueno, I. Zagorac, T. Mondejar, J. Sanchez, S. Mourón, J. Muñoz, G. Gómez-López, V. Jimenez-Renard, F. Mulero, N.S. Chandel, M. Quintela-Fandino, Targeting Tumor Mitochondrial Metabolism Overcomes Resistance to Antiangiogenics, Cell Rep. 15 (2016) 2705–2718. https://doi.org/10.1016/j.celrep.2016.05.052.

[60] Y. Chen, L. Pan, M. Jiang, D. Li, L. Jin, Nanostructured lipid carriers enhance the bioavailability and brain cancer inhibitory efficacy of curcumin both in vitro and in vivo, Drug Deliv. 23(4) (2015) 1–10. https://doi.org/10.3109/10717544.2015.1049719.

[61] J. Emami, M. Rezazadeh, H. Sadeghi, K. Khadivar, Development and optimization of transferrin-conjugated nanostructured lipid carriers for brain delivery of paclitaxel using Box–Behnken design, Pharm. Dev. Technol. 22 (2017) 370–382. https://doi.org/10.1080/10837450.2016.1189933.

[62] X. Zhu, H. Zhou, Y. Liu, Y. Wen, C. Wei, Q. Yu, J. Liu, Transferrin/aptamer conjugated mesoporous ruthenium nanosystem for redox-controlled and targeted chemo-photodynamic therapy of glioma, Acta Biomater. 82 (2018) 143–157. https://doi.org/10.1016/j.actbio.2018.10.012.

[63] L. Gastaldi, L. Battaglia, E. Peira, D. Chirio, E. Muntoni, I. Solazzi, M. Gallarate, F. Dosio, Solid lipid nanoparticles as vehicles of drugs to the brain: Current state of the art, Eur. J. Pharm. Biopharm. (2014). https://doi.org/10.1016/j.ejpb.2014.05.004.

[64] Y. Shen, Y. Lu, M. Jv, J. Hu, Q. Li, J. Tu, Enhancing effect of Labrasol on the intestinal absorption of ganciclovir in rats, Drug Dev. Ind. Pharm. 37 (2011) 1415–1421. https://doi.org/10.3109/03639045.2011.582874.

[65] O.Z. Fisher, N.A. Peppas, Quantifying tight junction disruption caused by biomimetic pH-sensitive hydrogel drug carriers, J. Drug Deliv. Sci. Technol. 18 (2008) 47–50. https://doi.org/10.1016/S1773-2247(08)50006-2.

[66] C. Guccione, M. Oufir, V. Piazzini, D.E. Eigenmann, E.A. Jähne, V. Zabela, M.T. Faleschini, M.C. Bergonzi, M. Smiesko, M. Hamburger, A.R. Bilia, Andrographolide-loaded nanoparticles for brain delivery: Formulation, characterisation and in vitro permeability using hCMEC/D3 cell line, Eur. J. Pharm. Biopharm. (2017).

https://doi.org/10.1016/j.ejpb.2017.06.018.

[67] B. Subramaniam, Z.H. Siddik, N.H. Nagoor, Optimization of nanostructured lipid carriers: understanding the types, designs, and parameters in the process of formulations, J. Nanoparticle Res. 22 (2020) 141. https://doi.org/10.1007/s11051-020-04848-0.

[68] B. Mukherjee, Preparation, characterization and in-vitro evaluation of sustained release protein-loaded nanoparticles based on biodegradable polymers, Int. J. Nanomedicine. 3(4) (2008) 487. https://doi.org/10.2147/IJN.S3938.

[69] C. Caddeo, K. Teskač, C. Sinico, J. Kristl, Effect of resveratrol incorporated in liposomes on proliferation and UV-B protection of cells, Int. J. Pharm. 363 (2008) 183–191. https://doi.org/10.1016/j.ijpharm.2008.07.024.

[70] A. Kim, W.B. Ng, W. Bernt, N.J. Cho, Validation of Size Estimation of Nanoparticle Tracking Analysis on Polydisperse Macromolecule Assembly, Sci. Rep. (2019). https://doi.org/10.1038/s41598-019-38915-x.

[71] D. Teleanu, C. Chircov, A. Grumezescu, A. Volceanov, R. Teleanu, Blood-Brain Delivery Methods Using Nanotechnology, Pharmaceutics. 10 (2018) 269. https://doi.org/10.3390/pharmaceutics10040269.

[72] E. Bobbi, B. Sabagh, S.-A. Cryan, J.A. Wilson, A. Heise, Anisotropic polymer nanoparticles with solvent and temperature dependent shape and size from triblock copolymers, Polym. Chem. 10 (2019) 3436–3443. https://doi.org/10.1039/C9PY00363K.

[73] M. V. Lozano, H. Esteban, J. Brea, M.I. Loza, D. Torres, M.J. Alonso, Intracellular delivery of docetaxel using freeze-dried polysaccharide nanocapsules, J. Microencapsul. 30 (2013) 181–188. https://doi.org/10.3109/02652048.2012.714411.

[74] M.N. Koopaei, M.R. Khoshayand, S.H. Mostafavi, M. Amini, M.R. Khorramizadeh, M.J. Tehrani, F. Atyabi, R. Dinarvand, Docetaxel loaded PEG-PLGA nanoparticles: Optimized drug loading, in-vitro cytotoxicity and in-vivo antitumor effect, Iran. J. Pharm. Res. 13(3) (2014) 819–834. https://doi.org/10.22037/ijpr.2014.1533.

[75] D. Liu, Z. Liu, L. Wang, C. Zhang, N. Zhang, Nanostructured lipid carriers as novel carrier for parenteral delivery of docetaxel, Colloids Surfaces B Biointerfaces. 85 (2011) 262–269.

https://doi.org/10.1016/j.colsurfb.2011.02.038.

[76] A.P. Meilakhs, S. V. Koniakhin, New explanation of Raman peak redshift in nanoparticles, Superlattices Microstruct. 110 (2016) 319–323. https://doi.org/10.1016/j.spmi.2017.08.010.

[77] S.S. Rohiwal, A.P. Tiwari, G. Verma, S.H. Pawar, Preparation and evaluation of bovine serum albumin nanoparticles for ex vivo colloidal stability in biological media, Colloids Surfaces A Physicochem. Eng. Asp. 480 (2015) 28–37. https://doi.org/10.1016/j.colsurfa.2015.04.017.

[78] T.M. Göppert, R.H. Müller, Adsorption kinetics of plasma proteins on solid lipid nanoparticles for drug targeting, Int. J. Pharm. 302 (2005) 172–186. https://doi.org/10.1016/j.ijpharm.2005.06.025.

[79] S. Honary, F. Zahir, Effect of Zeta Potential on the Properties of Nano-Drug Delivery Systems - A Review (Part 2), Trop. J. Pharm. Res. 12 (2013) 265–273. https://doi.org/10.4314/tjpr.v12i2.20.

[80] N. Nordin, S.K. Yeap, H.S. Rahman, N.R. Zamberi, N. Abu, N.E. Mohamad, C.W. How, M.J. Masarudin, R. Abdullah, N.B. Alitheen, In vitro cytotoxicity and anticancer effects of citral nanostructured lipid carrier on MDA MBA-231 human breast cancer cells, Sci. Rep. 9 (2019) 1614. https://doi.org/10.1038/s41598-018-38214-x.

[81] X. Liu, Q. Jin, Y. Ji, J. Ji, Minimizing nonspecific phagocytic uptake of biocompatible gold nanoparticles with mixed charged zwitterionic surface modification, J. Mater. Chem. 22 (2012) 1916–1927. https://doi.org/10.1039/C1JM14178C.

[82] E.L. da Rocha, L.M. Porto, C.R. Rambo, Nanotechnology meets 3D in vitro models: Tissue engineered tumors and cancer therapies, Mater. Sci. Eng. C. 34 (2014) 270–279. https://doi.org/10.1016/j.msec.2013.09.019.

[83] N.K.Y. Wong, R.A. Shenoi, S. Abbina, I. Chafeeva, J.N. Kizhakkedathu, M.K. Khan, Nontransformed and Cancer Cells Can Utilize Different Endocytic Pathways to Internalize Dendritic Nanoparticle Variants: Implications on Nanocarrier Design, Biomacromolecules. 18(8) (2017) 2427–2438. https://doi.org/10.1021/acs.biomac.7b00590.

[84] G. Sahay, D.Y. Alakhova, A. V. Kabanov, Endocytosis of nanomedicines, J. Control. Release. 18(1) (2010) 1–22. https://doi.org/10.1016/j.jconrel.2010.01.036.

[85] C. Caoduro, E. Hervouet, C. Girard-Thernier, T. Gharbi, H. Boulahdour, R. Delage-Mourroux, M. Pudlo, Carbon nanotubes as gene carriers: Focus on internalization pathways related to functionalization and properties, Acta Biomater. 49 (2017) 36–44. https://doi.org/10.1016/j.actbio.2016.11.013.

[86] E. Silva, L. Barreiros, M.A. Segundo, S.A. Costa Lima, S. Reis, Cellular interactions of a lipid-based nanocarrier model with human keratinocytes: Unravelling transport mechanisms, Acta Biomater. 53 (2017) 439–449. https://doi.org/10.1016/j.actbio.2017.01.057.

[87] S. Shubber, D. Vllasaliu, C. Rauch, F. Jordan, L. Illum, S. Stolnik, Mechanism of Mucosal Permeability Enhancement of CriticalSorb® (Solutol® HS15) Investigated In Vitro in Cell Cultures, Pharm. Res. 32 (2015) 516–527. https://doi.org/10.1007/s11095-014-1481-5.

[88] A.W.G. Alani, D.A. Rao, R. Seidel, J. Wang, J. Jiao, G.S. Kwon, The Effect of Novel Surfactants and Solutol® HS 15 on Paclitaxel Aqueous Solubility and Permeability Across a Caco-2 Monolayer, J. Pharm. Sci. 99 (2010) 3473–3485. https://doi.org/10.1002/jps.22111.

[89] P. BLASI, S. GIOVAGNOLI, A. SCHOUBBEN, M. RICCI, C. ROSSI, Solid lipid nanoparticles for targeted brain drug delivery☆, Adv. Drug Deliv. Rev. 59 (2007) 454–477. https://doi.org/10.1016/j.addr.2007.04.011.

[90] Z. Miao, Y. Dong, W. Fang, D. Shang, D. Liu, K. Zhang, B. Li, Y.-H. Chen, VEGF Increases Paracellular Permeability in Brain Endothelial Cells via Upregulation of EphA2, Anat. Rec. 297 (2014) 964–972. https://doi.org/10.1002/ar.22878.

[91] H. YUAN, J. MIAO, Y. DU, J. YOU, F. HU, S. ZENG, Cellular uptake of solid lipid nanoparticles and cytotoxicity of encapsulated paclitaxel in A549 cancer cells, Int. J. Pharm. 348 (2008) 137–145. https://doi.org/10.1016/j.ijpharm.2007.07.012.

[92] K.M.R. Srivalli, P.K. Lakshmi, Overview of P-glycoprotein inhibitors: a rational outlook, Brazilian J. Pharm. Sci. 48 (2012) 353–367. https://doi.org/10.1590/S1984-82502012000300002.

[93] A. Marino, A. Camponovo, A. Degl'Innocenti, M. Bartolucci, C. Tapeinos, C. Martinelli, D. De Pasquale, F. Santoro, V. Mollo, S. Arai, M. Suzuki, Y. Harada, A. Petretto, G. Ciofani,

Multifunctional temozolomide-loaded lipid superparamagnetic nanovectors: dual targeting and disintegration of glioblastoma spheroids by synergic chemotherapy and hyperthermia treatment, Nanoscale. 11 (2019) 21227–21248. https://doi.org/10.1039/C9NR07976A.

[94] J. Bicker, G. Alves, A. Fortuna, A. Falcão, Blood–brain barrier models and their relevance for a successful development of CNS drug delivery systems: A review, Eur. J. Pharm. Biopharm. 87 (2014) 409–432. https://doi.org/10.1016/j.ejpb.2014.03.012.

[95] J.C. Fontoura, C. Viezzer, F.G. dos Santos, R.A. Ligabue, R. Weinlich, R.D. Puga, D. Antonow, P. Severino, C. Bonorino, Comparison of 2D and 3D cell culture models for cell growth, gene expression and drug resistance, Mater. Sci. Eng. C. 107 (2020) 110264. https://doi.org/10.1016/j.msec.2019.110264.

[96] A.-J. LI, Y.-H. ZHENG, G.-D. LIU, W.-S. LIU, P.-C. CAO, Z.-F. BU, Efficient delivery of docetaxel for the treatment of brain tumors by cyclic RGD-tagged polymeric micelles, Mol. Med. Rep. 11 (2015) 3078–3086. https://doi.org/10.3892/mmr.2014.3017.

[97] R. Wen, B. Banik, R.K. Pathak, A. Kumar, N. Kolishetti, S. Dhar, Nanotechnology inspired tools for mitochondrial dysfunction related diseases, Adv. Drug Deliv. Rev. 99 (2016) 52–69. https://doi.org/10.1016/j.addr.2015.12.024.

[98] S. Wen, D. Zhu, P. Huang, Targeting cancer cell mitochondria as a therapeutic approach, Future Med. Chem. 5 (2013) 53–67. https://doi.org/10.4155/fmc.12.190.

[99] T.A. Bhat, S. Kumar, A.K. Chaudhary, N. Yadav, D. Chandra, Restoration of mitochondria function as a target for cancer therapy, Drug Discov. Today. 20 (2015) 635–643. https://doi.org/10.1016/j.drudis.2015.03.001.

[100] B. García-Pinel, C. Porras-Alcalá, A. Ortega-Rodríguez, F. Sarabia, J. Prados, C. Melguizo, J.M. López-Romero, Lipid-Based Nanoparticles: Application and Recent Advances in Cancer Treatment, Nanomaterials. 9 (2019) 638. https://doi.org/10.3390/nano9040638.

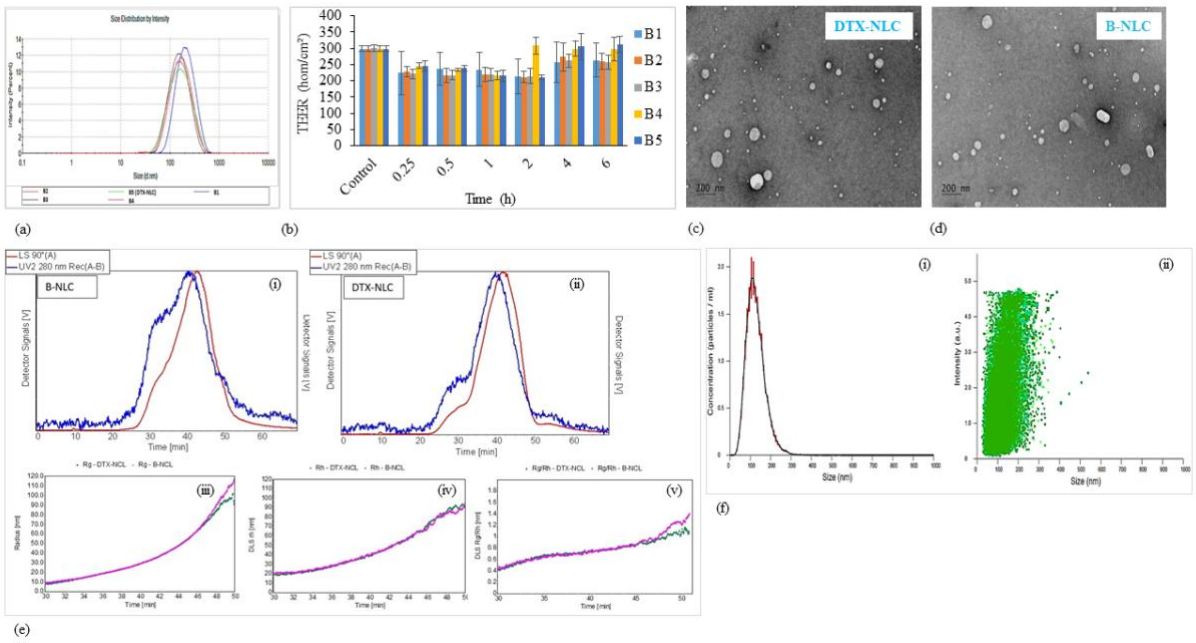

Fig. 1. (a) Particle size distribution overlay graph for B1, B2, B3, B4 and B5 (DTX-NLC) formulations, (b) Change in TEER values observed in in-vitro 3D Blood brain barrier model on treatment with five NLCs formulations, Transmission electron microscopy (TEM) images for (c) DTX-NLC and (d) B-NLC, (e) Asymmetric Flow Field-Flow Fractionation graphs for (i) B-NLC and (ii) DTX-NLC with their radius of gyration (Rg) and hydrodynamic radius (Rh), the detector signals from light scattering (MALS 90◦, red) and UV (280 nm, blue), (iii) Comparison of size distribution of Rg for DTX-NLC and B-NLC, (iv) Comparison of size distribution of Rh for DTX-NLC and B-NLC and (v) the ratio of Rg/Rh that indicates the shape or conformation changes, (f) Nanoparticle Tracking Analysis (NTA) of DTX-NLC (i) the averaged Concentration vs. Size plot and (ii) Intensity vs. Size graph. Data is presented as mean ± SD, n = 3. Docetaxel (DTX), Docetaxel loaded nanostructured lipid carrier (DTX-NLC), blank nanostructured lipid carrier (B-NLC). (For interpretation of the references to colour in this figure legend, the reader is referred to the web version of this article.).

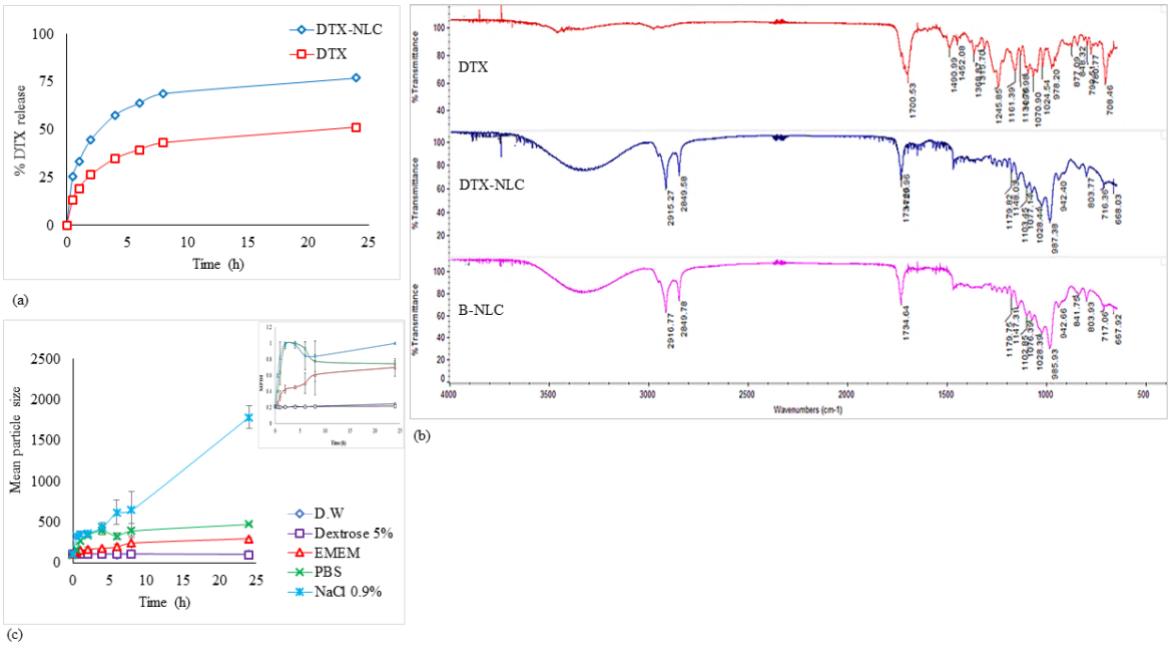

Fig. 2. (a) DTX release vs. time profile for DTX-NLC and DTX (dispersed in 1% Tween 80) over 24 h at 37 ◦C in 30% ethanol + 70% PBS, (pH 7.4) dissolution media, (b) FTIR spectrum and characteristic peaks for DTX, DTX-NLC and B-NLC, (c) Colloidal stability and effect of incubation in physiological media on particle size and PDI [Inset] of DTX-NLCs over 24 h at 37 ◦C with PBS, EMEM, Dextrose 5%, NaCl 0.9% and purified water. Docetaxel loaded nanostructured lipid carrier (DTX-NLC), blank nanostructured lipid carrier (B-NLC); PBS Phosphate buffer saline; EMEM Eagle's minimum essential medium.

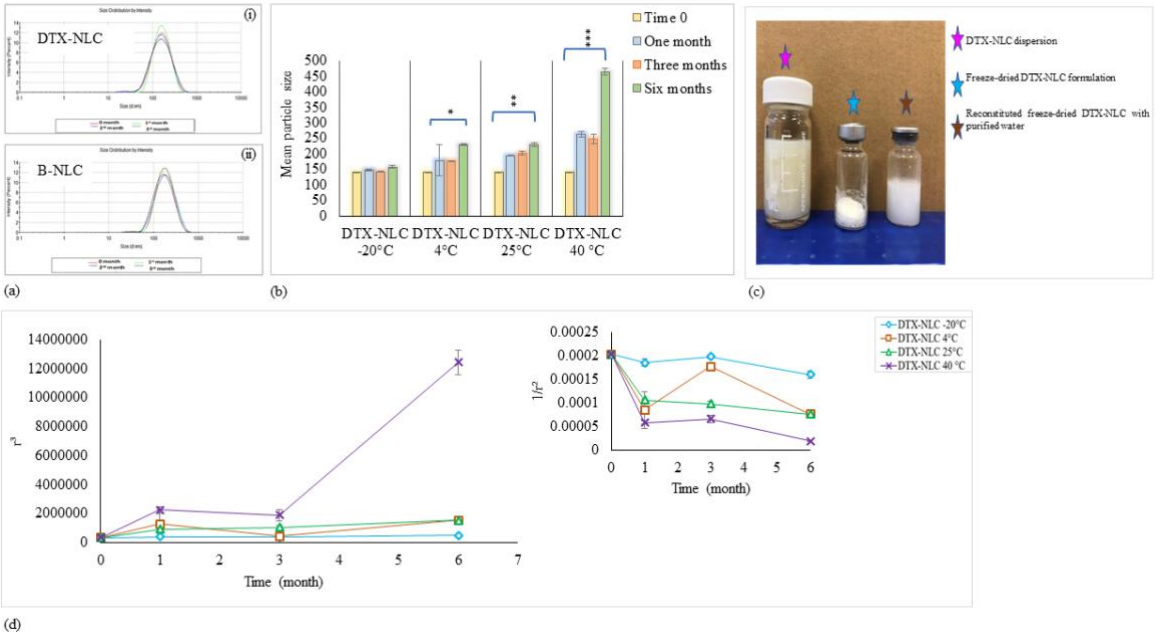

Fig. 3. (a) Short-term stability studies, overlay graphs of particle size and size distribution for (i) DTX-NLC and (ii) B-NLC stored for three months at room temperature, (b) Long-term stability study over six months and the effect of storing the DTX-NLCs at - 20, 4, 25, and 40 ◦C on mean particle size, (c) DTX-NLC formulation freshly prepared in comparison to freeze dried form, and reconstituted freeze dried formulation with purified water, (d) the plot of r^3 and $1/r^2$ [inset] as a function of time. p-Value refer to significant difference *p < 0.05, **p < 0.01, and ***p < 0.00. Data is presented as mean ± SD (n = 3). Docetaxel loaded nanostructured lipid carrier (DTX-NLC), blank nanostructured lipid carrier (B-NLC) and the radius of NLCs refer to as r.

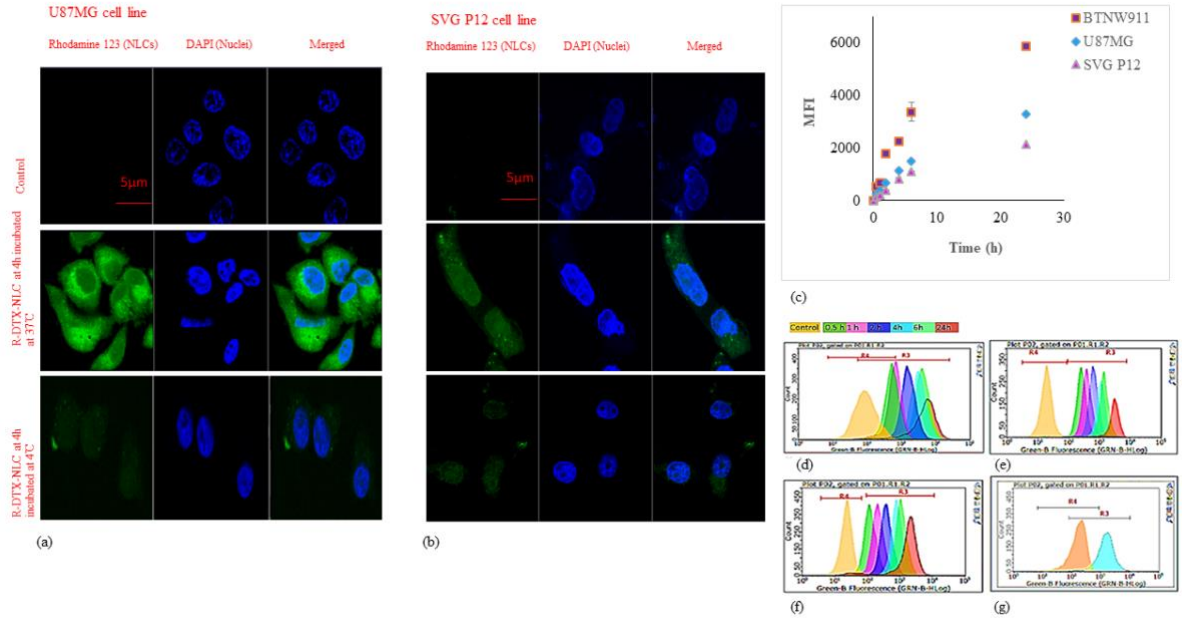

Fig. 4. Confocal microscopy images showing cellular internalisation of R-DTX-NLC after 4 h incubation at 37 ◦C and 4 ◦C for (a) U87MG and (b) SVG P12 cells, the blue fluorescence refers to the stained nucleus with DAPI, and the green fluorescence refers to the Rhodamine 123 labelled docetaxel nanostructured lipid carrier (DTX-NLC), the control is the untreated cell lines, (c) Time-dependent uptake of Rhodamine 123 labelled DTX-NLC in BTNW911, U87MG, and SVG P12 cells when incubated over a period of 24 h. Flow cytometer histograms of (d) BTNW911, (e) U87MG, (f) SVG P12 and (g) RAW 264.7 cells after treatment with Rhodamine 123 labelled DTX-NLC. R4 represents the region of untreated control cells, and R3 represents the region of shifted peaks as the fluorescence intensity increases the peaks shift more to the right over time as evidence of increased uptake with time. Data is presented as mean ± SD n = 3. (For interpretation of the references to colour in this figure legend, the reader is referred to the web version of this article).

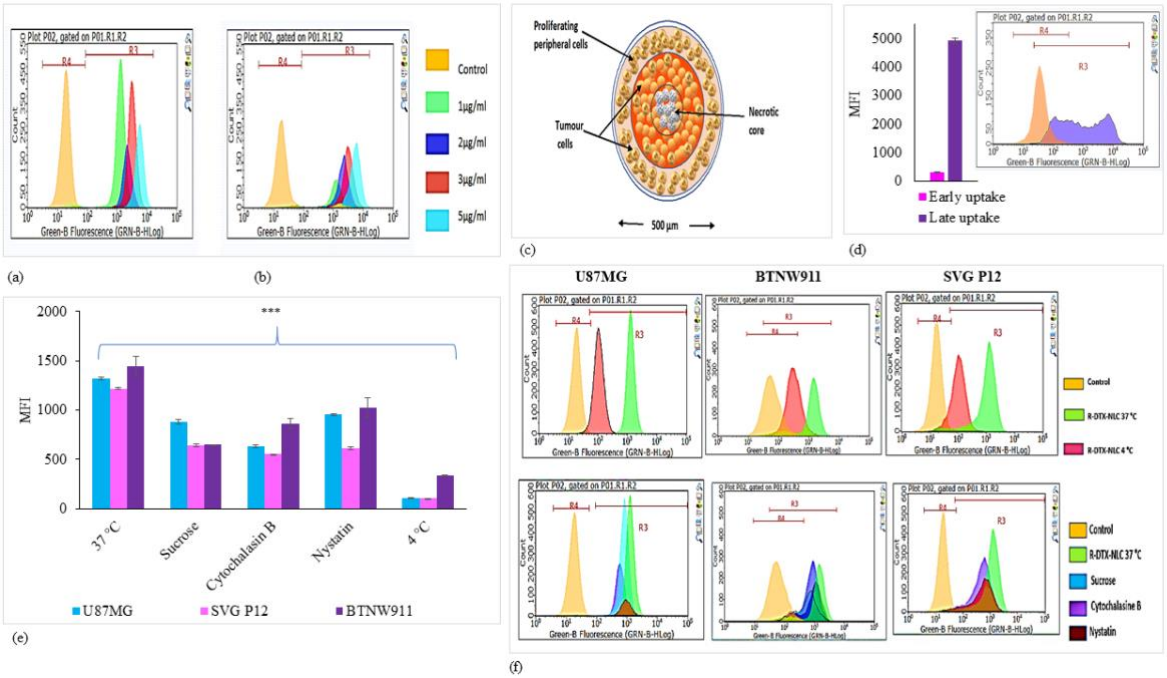

Fig. 5. (a) Flow cytometer histograms for concentration-dependent uptake of Rhodamine 123 labelled DTX-NLC in U87MG cells, (b) Concentration-dependent uptake in SVG P12 cells, (c) Illustration for 3D tumour spheroids (d) Bar chart and flow cytometer histograms for Rhodamine 123 labelled DTX-NLC at 1 μ g/ml concentration incubated for 6 h in 3D spheroids of U87MG cells, (e) Determination of endocytosis pathways following treatment of U87MG, BTNW911 and SVG P12 cell lines with various inhibitors, graph displaying mean fluorescence intensity (MFI) bar chart (f) Flow cytometer histograms before and after incubation with Rhodamine 123 labelled DTX-NLC in the presence of inhibitors. Untreated cell lines referred to region R4 for the control and R3 represents a region around the shifted peaks. p-Value refer to significant difference ***p < 0.00. Data is presented as mean ± SD (n = 3). R-DTX-NLC (Rhodamine 123 (R) loaded within the docetaxel nanostructured lipid carrier (DTX-NLC)).

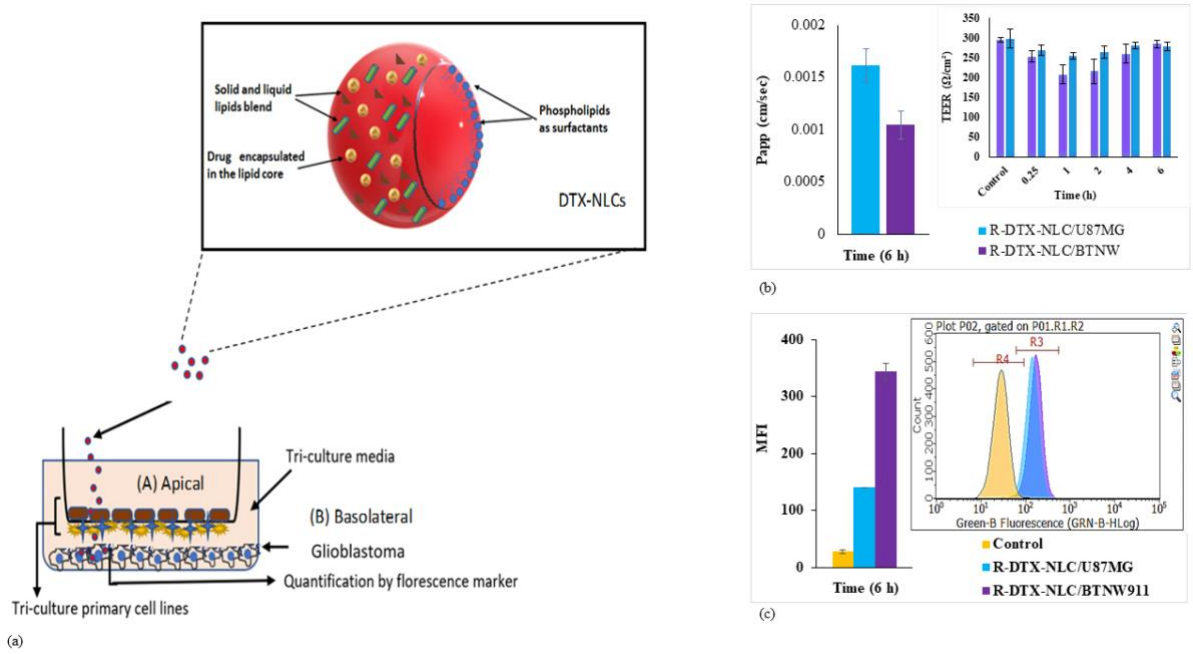

Fig. 6. Permeability and cell uptake data following penetration through 3D in-vitro BBTB model (a) illustration of DTX-NLCs permeability through 3D BBTB model, (b) TEER and Papp values after treatment with Rhodamine 123 labelled DTX-NLC through BBTB model in the presence of glioblastoma short-term culture BTNW911 and immortalised U87MG cell lines, (c) MFI bar chart and flow cytometer histograms demonstrating the uptake of DTX-NLCs in glioblastoma short-term culture BTNW911 and immortalised U87MG cell lines, and peak shifts following 6 h incubation time, control (untreated cells); U87MG and BTNW911 cells . Data are given as mean ± SD (n = 3).
R-DTX-NLC (Rhodamine 123 (R) loaded within the docetaxel nanostructured lipid carrier (DTX-NLC).

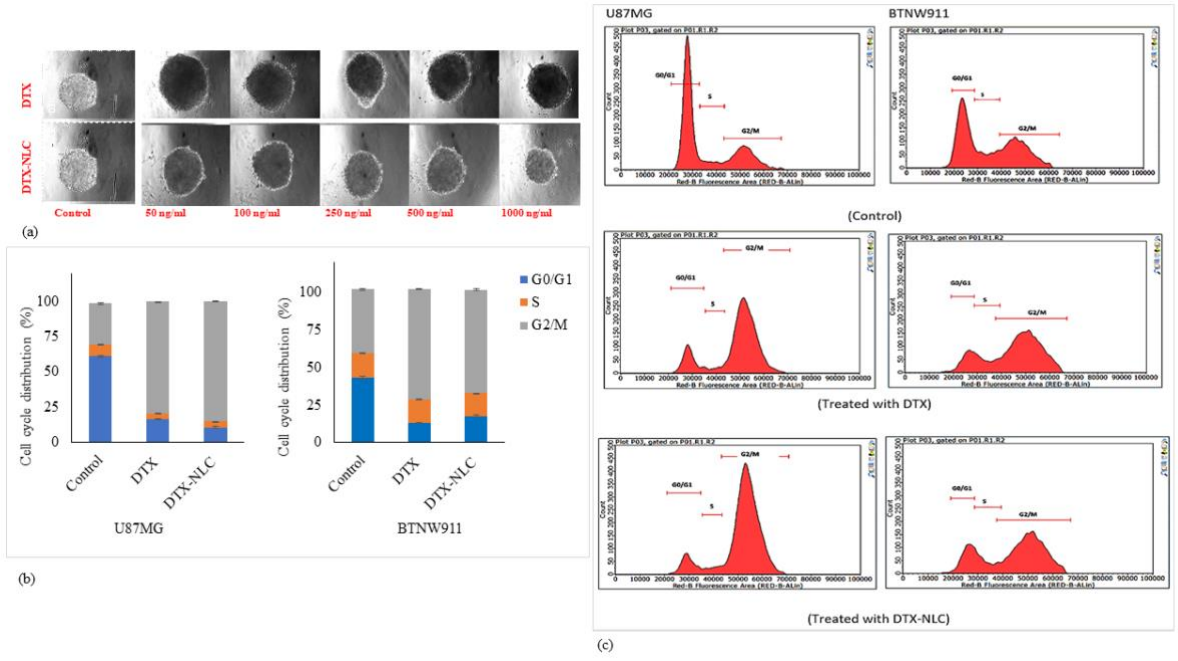

Fig. 7. (a) Light microscopy images of U87MG spheroids when treated with DTX and DTX-NLC at a range of concentrations between 50 and 1000 ng/ml and incubated for 72 h (b) Cell cycle distribution for control (untreated cells), DTX and DTX-NLC treated U87MG and BTNW911 cells after 24 h incubation. (c) Flow cytometer histograms of cell cycle distribution for control (untreated cells), DTX and DTX-NLC treated U87MG and BTNW911 cells after 24 h incubation. Data is presented as mean ± SD (n = 3).
Docetaxel (DTX), Docetaxel loaded nanostructured lipid carrier (DTX-NLC).

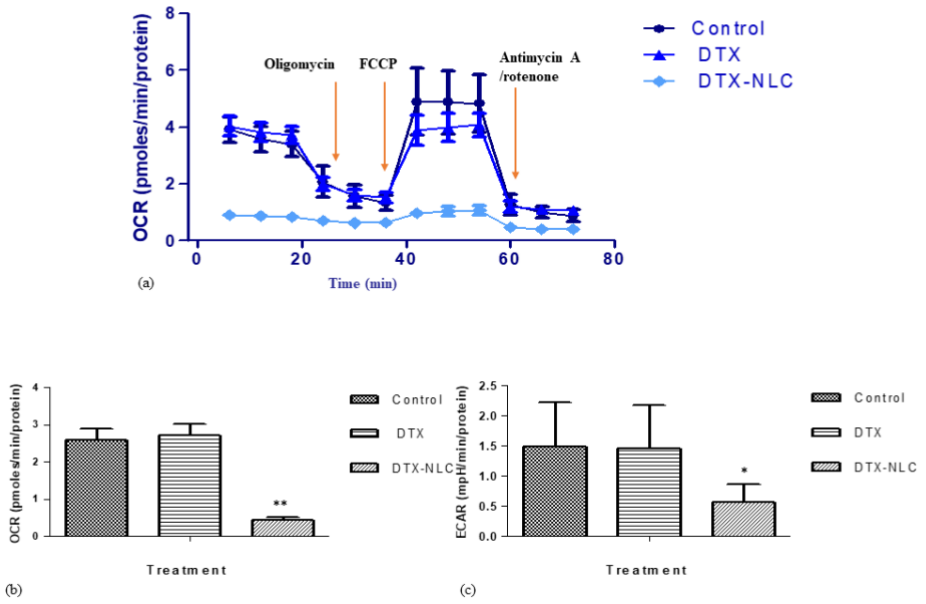

Fig. 8. Mitochondrial activity profiles and the effect of DTX and DTX-NLC on mitochondrial oxygen consumption rates (OCR) of U87MG cells (a-c) Breakdown of process-specific OCR/ECAR after sequential addition of XF Cell Mito Stress Test Kit (Oligomycin, Carbonyl cyanide-4 (trifluoromethoxy) phenylhydrazone (FCCP), and antimycin A/rotenone). p-Value refer to significant difference (*p < 0.05 and **p < 0.01). Data are mean/ ± SD, (n = 4).
Docetaxel loaded nanostructured lipid carrier (DTX-NLC), blank nanostructured lipid carrier (B-NLC).

Table 1. Compositions of Docetaxel loaded nanostructured lipid carrier DTX-NLC dispersions with four different liquid lipids.

Batch number	Lauroglycol 90 (mg)	Labrasol® (mg)	Capryol® propylene glycol monocaprylate (mg)	Kolliphor®HS15 (mg)
B1	-	750	-	-
B2	750	-	-	-
B3	-	-	750	-
B4	-	-	-	750
B5	150	150	150	300

Table 2. Physicochemical Characterisation of Blank and Docetaxel loaded nanostructured lipid carrier DTX-NLC formulations.

Formulations	B1	B2	B3	B4	B5	B-NLC
Particle Size (nm)	135.000 ±0.472	183.600 ±3.132	147.000 ±2.196	112.500 ±3.004	123.300 ±0.642	147.400 ±0.280
Polydispersity index	0.226 ±0.015	0.178 ±0.014	0.197 ±0.004	0.226 ±0.002	0.234 ±0.016	0.231 ±0.230
Zeta potential (mV)	-31.800 ±0.924	-28.700 ±2.510	-30.100 ±0.208	-26.000 ±0.100	-32.400 ±0.967	-34.400 ±0.870
Eentrapment efficiency (Percent)	94.750 ±0.850	99.230 ±0.170	99.510 ±0.200	99.510 ±0.150	99.130 ± 1.200	-
Total drug (Percent)	77.670 ±0.470	71.640 ±0.430	54.660 ±0.550	57.650 ±0.100	88.600 ±1.370	-
Drug loading (Percent)	1.940 ±0.012	1.700 ±0.430	1.360 ±0.002	1.440 ±0.120	2.010 ±0.034	-
Papp (cm/sec)	1.9×10^{-3} ±0.00013	1.7×10^{-3} ±0.00020	2.4×10^{-3} ±0.00037	2.4×10^{-3} ±0.00015	2×10^{-3} ±0.00013	-
Evans Blue concentration (µg/ml)	0.00100 ±0.00035	0.00450 ±0.00030	0.00810 ±0.00050	0.00025 ±0.00009	0.00020 ±0.00010	-

All values expressed as Mean ±SD.

Table 3. B-NLC and DTX-NLC DLS (Rh) and Rg data acquired by Asymmetric Flow Field-Flow Fractionation.

Formulation	Batch DLS Rh (nm)	Rg MALS (nm)	Flow DLS Rh (nm)
B-NLC	41.5	50.9	41.3
DTX-NLC	40.7	40.6	40.2

Rg- radius of gyration; Rh hydrodynamic radius, Docetaxel loaded nanostructured lipid carrier (DTX-NLC), blank nanostructured lipid carrier (B-NLC).

Table 4. DTX-NLCs and B-NLC in liquid dispersion stability study for three months at room temperature.

DTX-NLCs	Particle size (nm)	Polydispersity index	Zeta potential (mV)	Entrapment efficiency (%)	Total drug (%)	Drug loading (%)
Day 0	123.300 ±0.642	0.234 ±0.234	-32.400 ±0.960	99.130 ± 1.200	88.600 ±1.370	2.010 ±0.030
One month	135.400 ±2.460	0.235 ±0.003	-32.400 ±0.900	98.010 ±0.730	71.230 ±2.100	1.780 ±2.010
Two months	130.500 ±1.700	0.240 ±0.010	-32.300 ±1.010	97.850 ±0.830	66.610 ±0.470	1.660 ±0.320
Three months	130.000 ±0.720	0.260 ±0.009	-33.600 ±0.960	96.400 ±0.200	64.360 ±0.550	1.600 ±0.450
B-NLCs	**Particle size (nm)**	**Polydispersity index**	**Zeta potential (mV)**	**Entrapment efficiency (%)**	**Total drug (%)**	**Drug loading (%)**
Day 0	147.400 ±0.280	0.231 ±0.230	-34.400 ±0.870	-	-	-
One month	151.400 ±3.710	0.209 ±0.010	-35.500 ±0.850	-	-	-
Two months	144.100 ±0.980	0.235 ±0.010	-38.500 ±2.170	-	-	-
Three months	142.800 ±0.620	0.230 ±0.001	-35.600 ±0.910	-	-	-

Docetaxel loaded nanostructured lipid carrier (DTX-NLC), blank nanostructured lipid carrier (B-NLC). All values expressed as Mean ±SD.

Table 5. Mean IC_{50} values for DTX, DTX-NLC and B-NLCs following 72 h incubation. Formulations compared to the standard treatment DTX.

Cell lines	IC_{50} Values (ng/ml)		
	DTX	**DTX-NLC**	**B-NLC**
U87MG	1.80 ±0.01	3.17 ±0.36	N/A
SVG P12	0.22 ±0.10	1.80 ±1.18	N/A
BTNW911	1.77 ±0.64	25.18 *** ±0.24	N/A
U87MG spheroids	12.74 ±0.83	3.60 * ±0.53	-

Formulations compared to the standard treatment Docetaxel (DTX). Docetaxel loaded nanostructured lipid carrier (DTX-NLC), blank nanostructured lipid carrier (B-NLC). All values expressed as Mean ±SD. *P* value refer to significant difference * $p < 0.05$, ** $p < 0.01$, and *** $p < 0.00$.

Supplementary data

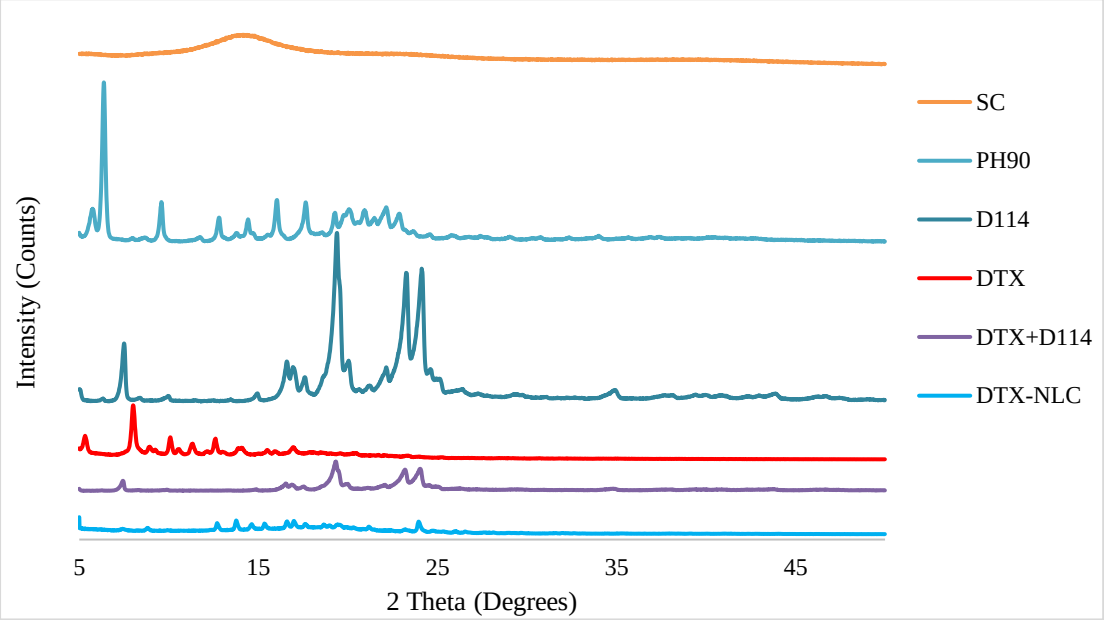

Fig S1 XRD structure of Sodium cholate (SC), Phospholipon H90 (PH90), DYNASAN114 (D114), Docetaxel (DTX), a physical mixture of drug and lipid (DTX and D114), and Docetaxel loaded nanostructured lipid carrier (DTX-NLC), expressed in 2Θ°.

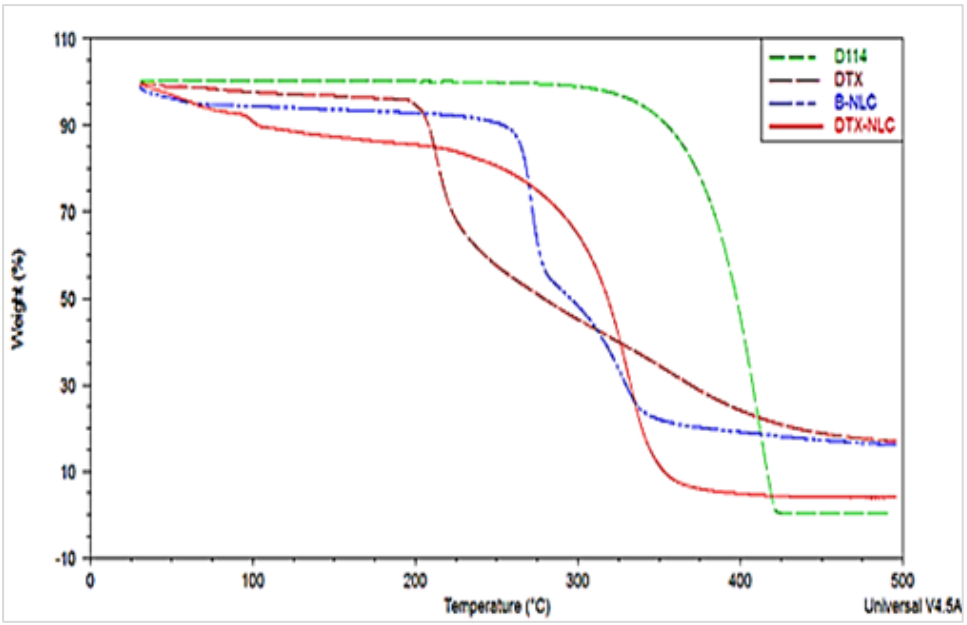

Fig S2 TGA thermographs using heat ranging from 25-500 °C for the overlay of Docetaxel (DTX), DYNASAN (D114), Docetaxel loaded nanostructured lipid carrier (DTX-NLC), blank nanostructured lipid carrier (B-NLC) degradation pattern.

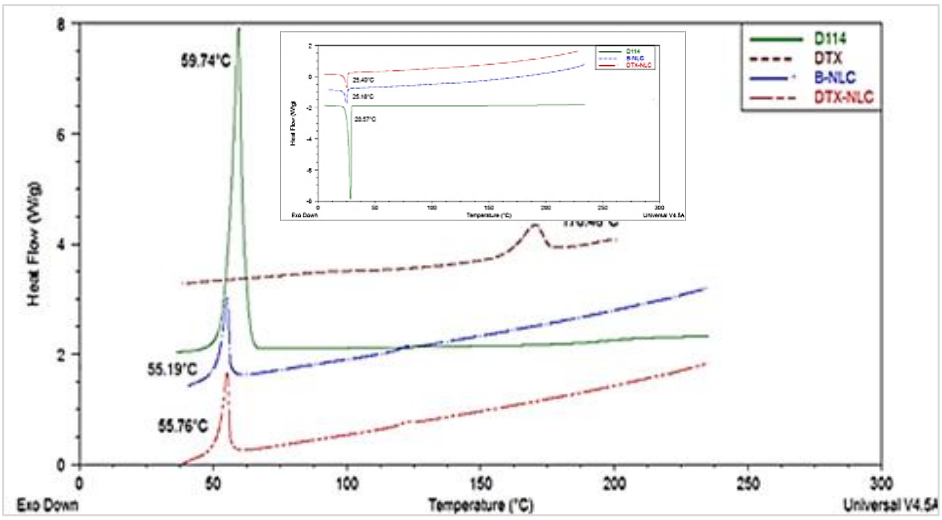

Fig S3 DSC thermograph showing melting and recrystallisation for DYNASAN (D114), Docetaxel (DTX) Docetaxel loaded nanostructured lipid carrier (DTX-NLC), blank nanostructured lipid carrier (B-NLC), using method heat/cool/heat.

Table S1 FTIR Vibrational band assignment for Docetaxel (DTX), Docetaxel loaded nanostructured lipid carrier (DTX-NLC), blank nanostructured lipid carrier (B-NLC).

FTIR frequency (cm^{-1})	Vibrational band assignment	DTX	DTX-NLC	B-NLC
3688	O-H stretching	√	√	
3459	N-H/ O-H stretching	√		
3326	N-H stretching		√	√ shift to 3351
2979	C-H stretching	√		
2915 and 2849	CH_2 asymmetrical and symmetrical stretching		√	√
1734	C=O stretching		√	√
1718	C=O stretching	√		
1700	C=O stretching	√	√	
1490	C=C stretching	√		
1472	CH_2 / CH_3 asymmetrical stretching		√	√
1457	N-H, CH_3, O-H diffraction	√	√	
1452	C-H bending	√		
1368	C-H bending/C-C stretching	√	√	
1273	C-O stretching		√	√
1254	C-O stretching		√	√
1245	C-O stretching	√		
1228	C-O stretching		√	√
1201	C-O stretching		√	√
1179	S=O stretching		√	√
1161	C-O stretching	√		
1148	S=O stretching		√	√
1103	C-N stretching		√	√
1077	CH_2 twisting/ aromatic ring stretching		√	√
1070	C-O stretching/ Aromatic ring stretch/CH_2 twisting	√		
1028	C-N /C-O stretching		√	√
1024	C-O stretching	√		
987	C=C bending		√	√
978	C-S stretching	√		
942	C-H twisting		√	√
848	C-H out of plane bending	√		
803	C=C bending		√	√
780	C-H bending	√		
716	C-H bending		√	√
708	C-H out of plane bending	√		
668	C=C bending/ Aromatic ring stretch		√	√

Table S2 Raman Vibrational band assignments for Docetaxel (DTX), Docetaxel loaded nanostructured lipid carrier (DTX-NLC).

Raman shift (cm^{-1})	Vibrational band assignment	DTX	DTX-NLC
1813	C=O stretching	√	√
1793	C=O	√	√
1786	C=C/C=O stretching	√	√ shifted to 1783
1651	C=O/ C=C stretching	√	√ shifted to 1658 high intensity
1631	C=O/C=C/ C=N stretching	√	√ shifted to 1626
1601	C=N/C=C stretching	√	√ shifted to 1605
1530	C-N stretching	√	√ shifted to 1533
1357	C-(NO2)	√	√
1346	C-(NO2) (phospholipids)	√	√
1275	C=O stretching	√	√ shifted to 1261
1230	C-N stretching/CH_2 twisting	√	√
1026	C=S	√	√ shifted to 1079
1003	C=S	√	√ shifted to 1061
960	C=O stretching	√	√
950	C-C stretching/ CH_2 rocking	√	√
894	C-C stretching	√	√ shifted to 908
849	C-C stretching	√	√ shifted to 842
702	C-N stretching	√	√
694	C-C/C=O deformation	√	√

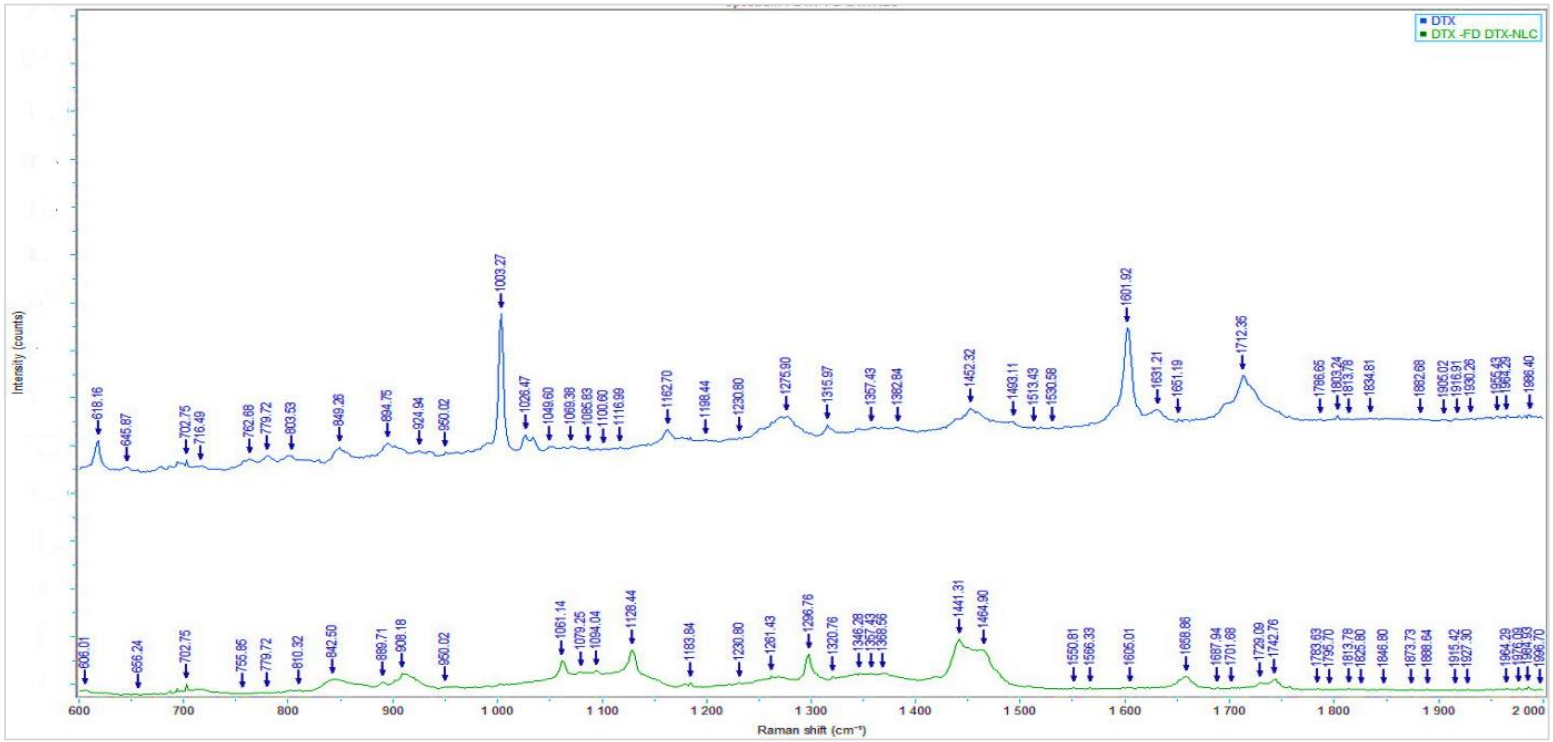

Fig S4 Raman overlay spectrum of Docetaxel (DTX) and Docetaxel loaded nanostructured lipid and their characteristic peaks.

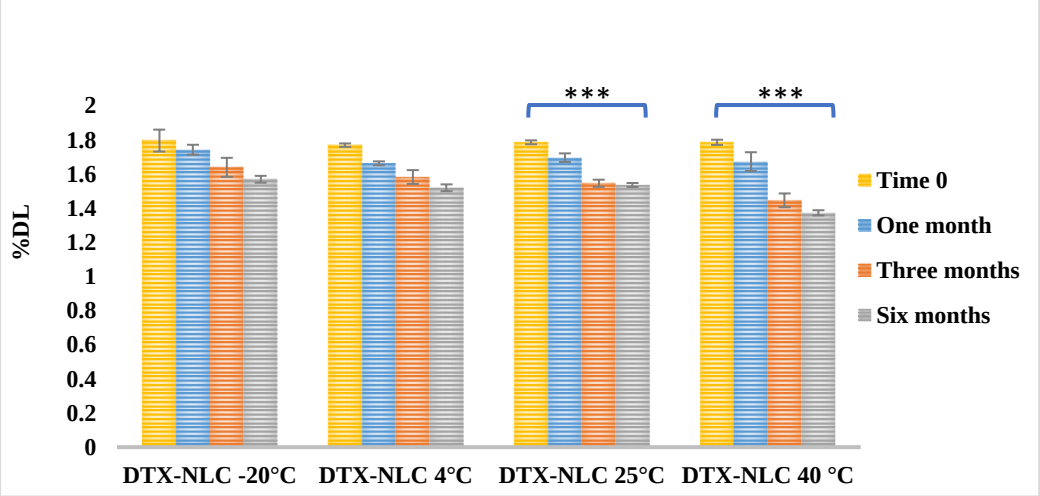

Fig S5 Stability study for freeze-dried formulation docetaxel loaded nanostructured lipid carrier (DTX-NLC) in various temperature and their effect on drug loading (%DL). *p-value* refer to very significant difference when *** $p < 0.000$. Data is presented as mean/±SD (n=3).

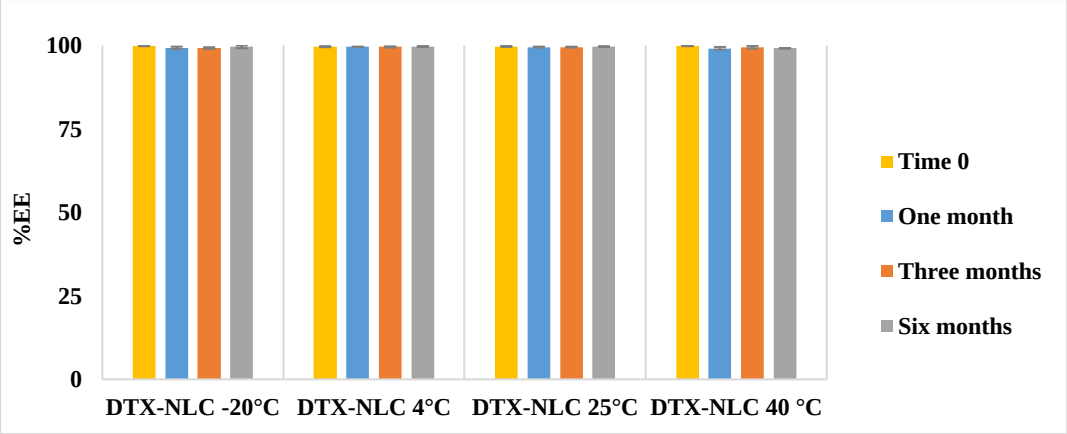

Fig S6 Stability study for freeze-dried formulation docetaxel loaded nanostructured lipid carrier (DTX-NLC) in various temperature and their effect on entrapment efficiency (%EE). *p-value* refer to very significant difference when *** $p < 0.000$. Data is presented as mean/±SD (n=3).

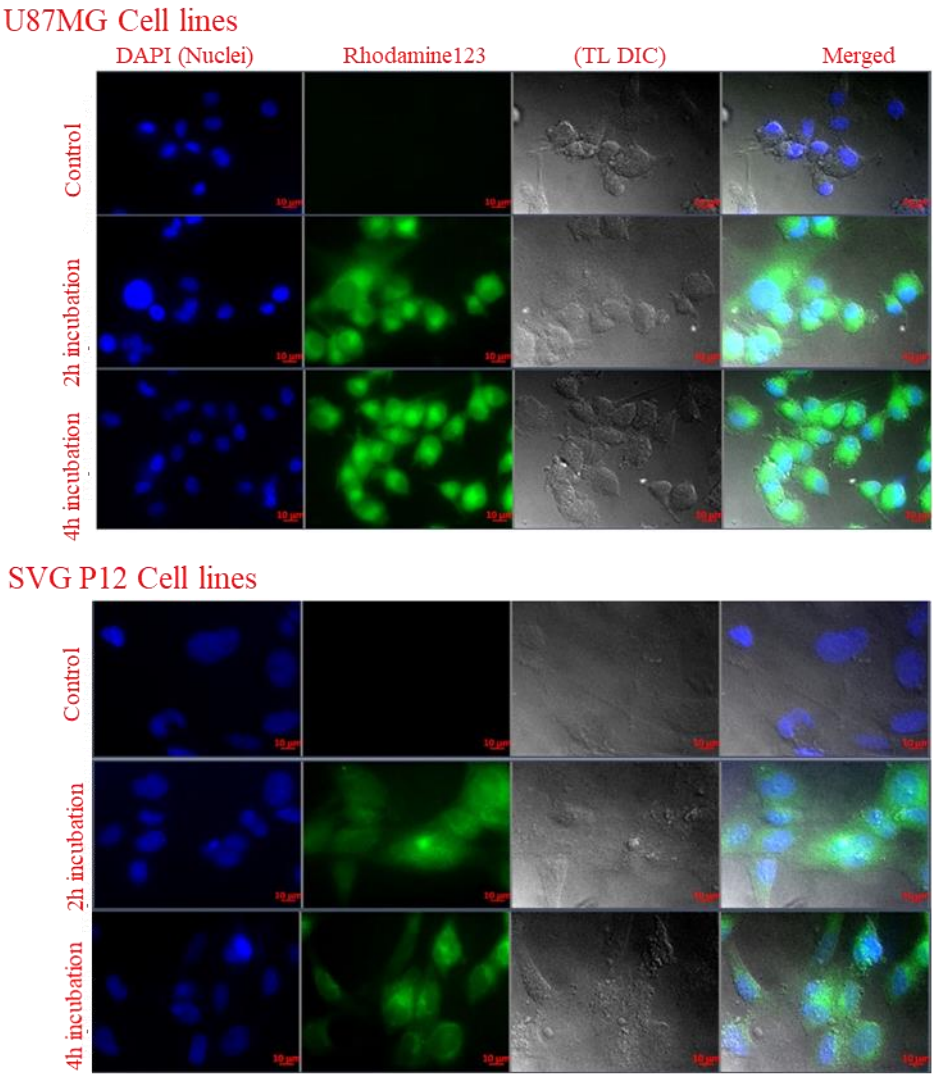

Fig S7 Fluorescence microscopy images showing cellular internalization of R-DTX-NLC after 2 and 4 h incubation in U87MG and SVG P12 cells, the blue fluorescence refers to the stained nucleus with DAPI, and the green fluorescence refers to the Rhodamine labelled docetaxel nanostructured lipid carrier (DTX-NLC), the control is the untreated cell lines

(U87MG Cell lines)

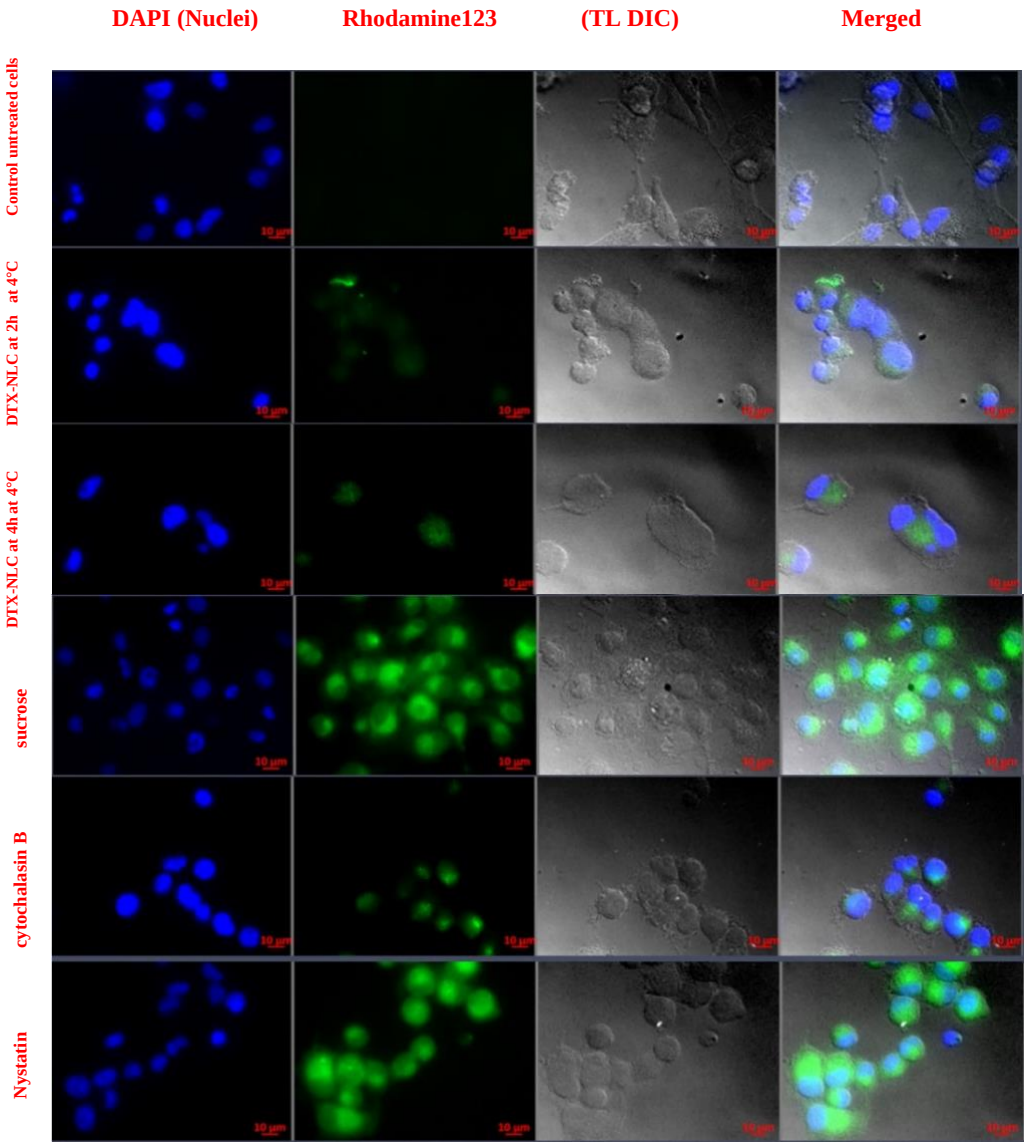

Fig S8 Quantitative pathway evaluation for Docetaxel loaded nanostructured lipid carrier (DTX-NLC) for U87MG cell lines when various pathway way inhibitors were evaluated. In this case untreated cells were used as a control.

SVG P12 Cell lines

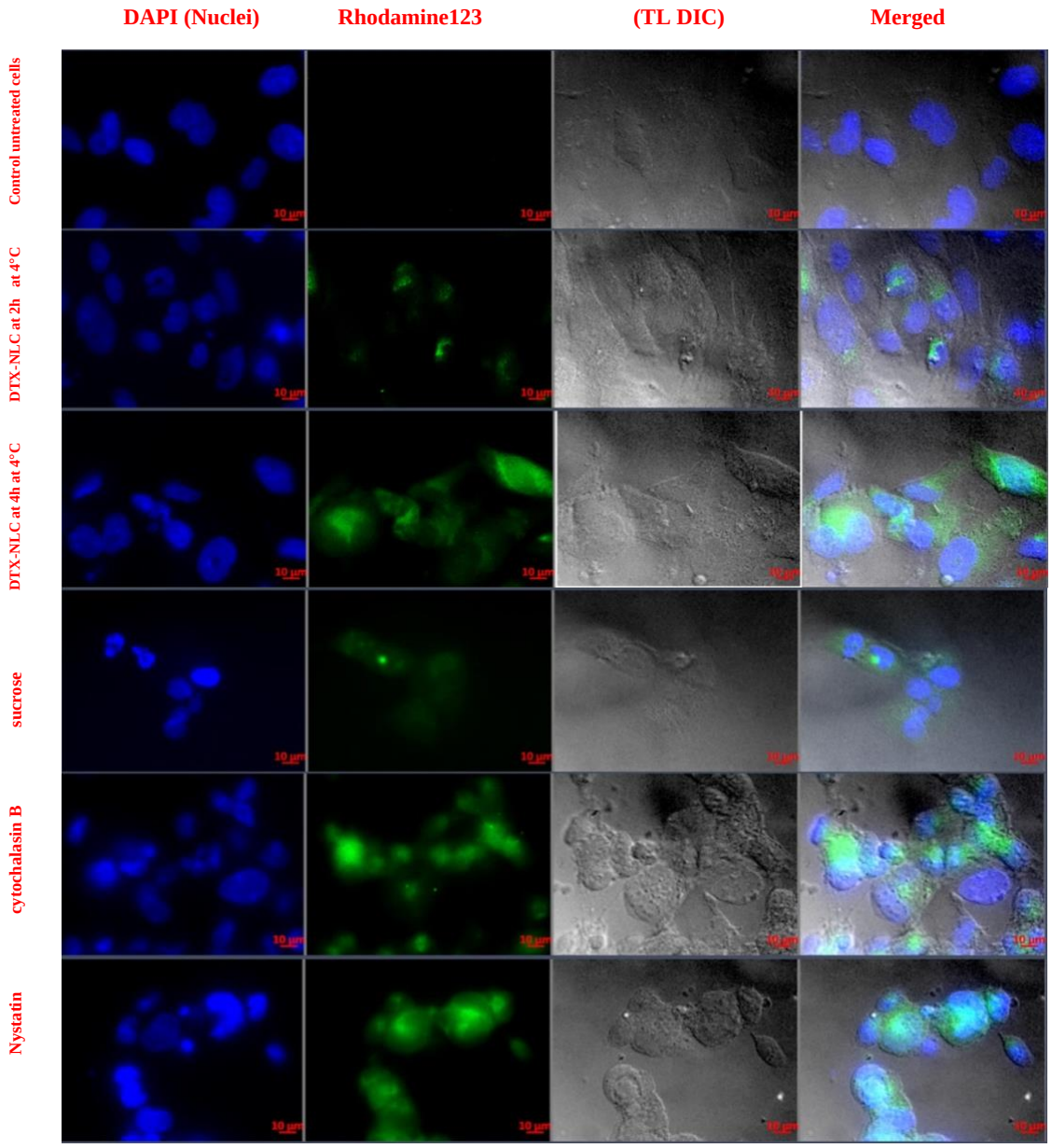

Fig S9 Qualitative pathway evaluation for Docetaxel loaded nanostructured lipid carrier (DTX-NLC) for SVG P12 cell lines when various pathway way inhibitors were evaluated. In this case untreated cells were used as a control.